

1 **Simulations of Energetic Neutral Atom sputtering from**
2 **Ganymede in preparation for the JUICE mission**

3 **A. Pontoni¹, M. Shimoyama¹, Y. Futaana¹, S. Fatemi², A. R. Poppe³, M.**
4 **Wieser¹, S. Barabash¹**

5 ¹Swedish Institute of Space Physics, Kiruna, Sweden

6 ²Department of Physics at Umeå University, Umeå, Sweden

7 ³Space Sciences Laboratory, University of California, Berkeley, CA, USA

8 **Key Points:**

- 9
- 10 • A new method for calculating sputtered fluxes at Ganymede is introduced
 - 11 • The energy spectra of sputtered H₂O, O₂, and H₂ ENAs are calculated for the first
12 time
 - 13 • The Jovian Neutrals Analyzer on JUICE can remotely map ion precipitation at
Ganymede

Abstract

Jovian magnetospheric plasma irradiates the surface of Ganymede and is postulated to be the primary agent that changes the surface brightness of Ganymede, leading to asymmetries between polar and equatorial regions as well as between the trailing and leading hemispheres. As impinging ions sputter surface constituents as neutrals, ion precipitation patterns can be remotely imaged using the Energetic Neutral Atoms (ENA) measurement technique. Here we calculate the expected sputtered ENA flux from the surface of Ganymede to help interpret future observations by ENA instruments, particularly the Jovian Neutral Analyzer (JNA) onboard the JUPITER ICy moon Explorer (JUICE) spacecraft. We use sputtering models developed based on laboratory experiments to calculate sputtered fluxes of H_2O , O_2 , and H_2 . The input ion population used in this study is the result of test particle simulations using electric and magnetic fields from a hybrid simulation of Ganymede's environment. This population includes a thermal component (H^+ and O^+ from 10 eV to 10 keV) and an energetic component (H^+ , O^{++} and S^{+++} from 10 keV to 10 MeV). We find a global ENA sputtering rate from Ganymede of $1.42 \times 10^{27} \text{ s}^{-1}$, with contributions from H_2 , O_2 , and H_2O of 34%, 17%, and 49% respectively. We also calculate the energy distribution of sputtered ENAs, give an estimate of a typical JNA count rate at Ganymede, and investigate latitudinal variations of sputtered fluxes along a simulated orbit track of the JUICE spacecraft. Our results demonstrate the capability of the JNA sensor to remotely map ion precipitation at Ganymede.

Plain Language Summary

Particles trapped by Jupiter's magnetic field interact with Jupiter's moons. Ganymede, the largest of those moons, lacks a dense atmosphere to protect its surface from these energetic Jovian particles, but Ganymede's magnetic field is strong enough to influence their trajectory: charged particles are deflected away from equatorial regions to polar regions, resulting in uneven particle precipitation patterns at the surface of Ganymede. When ions hit the surface of Ganymede, they eject particles from the surface, in a process referred to as sputtering. Those particles are mostly neutral and therefore unaffected by Ganymede's magnetic fields, so we can image where ions hit the surface of Ganymede by measuring ejected neutral particles. The Jovian Neutrals Analyzer (JNA) will fly onboard the JUPITER ICy moon Explorer (JUICE) spacecraft and will measure sputtered neutrals in the vicinity of Ganymede. To help interpret the data to be collected by JNA, we used models derived from laboratory experiments to simulate what JNA will observe at Ganymede. Our results show that JNA will be able to show us where ions hit the surface of Ganymede, which is important as uneven ion precipitation is thought to explain why Ganymede's poles are brighter than its equatorial regions.

1 Introduction

Imaging plasma precipitation patterns at the surface of Ganymede is a key measurement for understanding the effect of Jovian plasma precipitation on the brightness and composition of the surface. Ganymede stands out as Jupiter’s largest moon and also the only moon in the Solar System to feature an intrinsic magnetic field, causing the formation of a small magnetosphere inside Jupiters much larger magnetosphere. Ganymede’s magnetic field locally impedes or enhances Jovian plasma access to its surface, resulting in variable precipitation patterns (Khurana et al., 2007; Fatemi et al., 2016; Poppe et al., 2018; Plainaki et al., 2020). Precipitating ions can be backscattered by the surface or cause surface constituents and radiolytic products to sputter. Backscattered and sputtered particles leave the surface mainly as neutral and with energies ranging from eV to MeV (Johnson, 1990).

Such neutral particles are usually referred to as Energetic Neutral Atoms (ENAs) (Gruntman, 1997). The trajectories of ENAs are not influenced by electric or magnetic fields and therefore preserve information about their original location and direction. Thus ENA measurements can and have been used to remotely map ion precipitation on airless bodies, where in-situ precipitating ion observation is not easily possible. For example, backscattered solar wind protons and sputtered oxygen atoms were observed at the Moon by the Interstellar Boundary EXplorer (IBEX) (McComas et al., 2009; Allegrini et al., 2013) and by CENA on Chandrayaan-1 (Wieser et al., 2009; Vorburger et al., 2014; Futaana et al., 2013). Ganymede will also be visited by an ENA instrument: the Jovian Neutrals Analyzer (JNA) will fly on-board the JUperiter ICy moon Explorer (JUICE) spacecraft.

To help interpret the data collected by JNA, estimates of ENA fluxes are needed, but require modelling of the sputtering process. The sputtering process has been widely studied because of its relevance for icy bodies such as Ganymede, Europa, and Enceladus. Their lack of a dense atmosphere leaves their surface exposed to ion precipitation, leading to the sputtering of surface constituents and radiolytic products. Along with other processes such as sublimation and photo-stimulated desorption, sputtering contributes to the creation of a neutral exosphere on several bodies (Cooper, 2001; Johnson et al., 2004; Marconi, 2007; Cassidy et al., 2010; Wurz et al., 2010).

While a comprehensive analytical description of the sputtering process is not currently available, sputtering has been extensively studied through laboratory experiments (Baragiola et al., 2003; Fam et al., 2008; Teolis et al., 2017; Galli et al., 2017, 2018). Several methods have been developed to calculate the sputtering yield of ions on icy surfaces as a function of projectile energy and species, incidence angle, and surface temperature (Johnson et al., 2004; Fam et al., 2008; Teolis et al., 2017). Such methods, or combinations of them, have been used extensively to simulate surface-plasma interactions at Europa (Vorburger, 2018; Plainaki et al., 2010, 2012) and Ganymede (Marconi, 2007; Turc et al., 2014; Plainaki et al., 2015; Shematovich, 2016; Leblanc et al., 2017; Poppe et al., 2018; Plainaki et al., 2020).

Here, we estimate sputtered ENA fluxes at the surface of Ganymede by applying models formulated by Fam et al. (2008), Johnson et al. (2004) and Teolis et al. (2017) to a population of incident Jovian plasma obtained through hybrid simulations by Poppe et al. (2018). This allows us to calculate the expected sputtered ENA fluxes of H₂O, H₂, and O₂ and to further apply the Thompson-Sigmund (Sigmund, 1969) law to calculate their energy distribution. By convolving JNA’s estimated geometric factor with the energy distribution, we give an expected JNA count rate in the vicinity of Ganymede. Finally we investigate latitudinal variations of the sputtered ENA fluxes by simulating a simplified orbit of the JUICE spacecraft around Ganymede.

2 Materials and Methods

2.1 Input population

The incident ion population is taken from a combination of three-dimensional hybrid simulations of Ganymede's magnetosphere and subsequent backwards-Liouville particle tracing through the hybrid electromagnetic fields (Fatemi et al., 2016; Poppe et al., 2018). They simulated the ion velocity distribution for the Galileo G8 flyby, when Ganymede was in the Jovian plasma sheet. The incident population used as an input for calculating the sputtered ENA flux in this study is comprised of three-dimensional velocity distribution functions for thermal O^+ and H^+ from 10 eV to 10 keV and energetic H^+ , O^{++} and S^{+++} from 10 keV to 10 MeV. The spatial resolution of the hybrid model is $1^\circ \times 1^\circ$ in latitude and longitude at the surface of Ganymede.

Figure 1 shows the resulting plasma precipitation pattern, i.e. a map of the ion flux integrated over all incident species, energies and angles. On the trailing hemisphere ($180^\circ - 360^\circ W$) of the equatorial regions, Ganymede's surface is shielded from Jovian plasma by Ganymede's intrinsic magnetic field. In contrast, intense precipitation is observed on the leading hemisphere of the equatorial regions ($0^\circ - 180^\circ W$), where plasma is accelerated back towards Ganymede by reconnection in the magnetotail (Fatemi et al., 2016; Poppe et al., 2018). The most intense flux is observed in the high-latitude cusp regions on the leading hemisphere, where open-closed magnetic field lines boundaries are located ($\pm 50^\circ - 60^\circ$ in latitude) (Poppe et al., 2018).

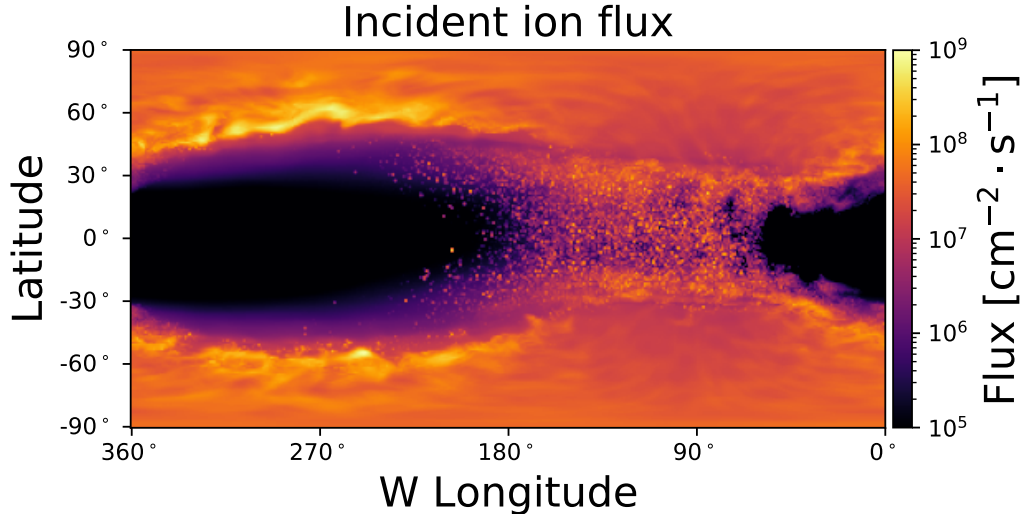


Figure 1. Incident ion flux at the surface of Ganymede, taken from Poppe et al. (2018) and integrated over all species, angles and energies. The leading hemisphere extends from $0^\circ W$ to $180^\circ W$ while the trailing hemisphere extends from $180^\circ W$ to $360^\circ W$. For our study here, we choose a single period along Ganymede's orbit such that the sub-solar point is located at $270^\circ W$, i.e. the co-rotating plasma flow is aligned with the sunlight direction.

Figure 2 shows the energy distribution of the incident ion flux at Ganymede's surface resulting from Poppe's backwards-Liouville tracing model. The flux was integrated over all incident angles and averaged over the surface of Ganymede. Two components can be identified: i) the thermal component comprised of plasma from Io's torus diffusing outwards (Siscoe & Summers, 1981); ii) the energetic component originating from accelerated Io torus plasma and solar wind plasma diffusing inwards (Siscoe et al., 1981).

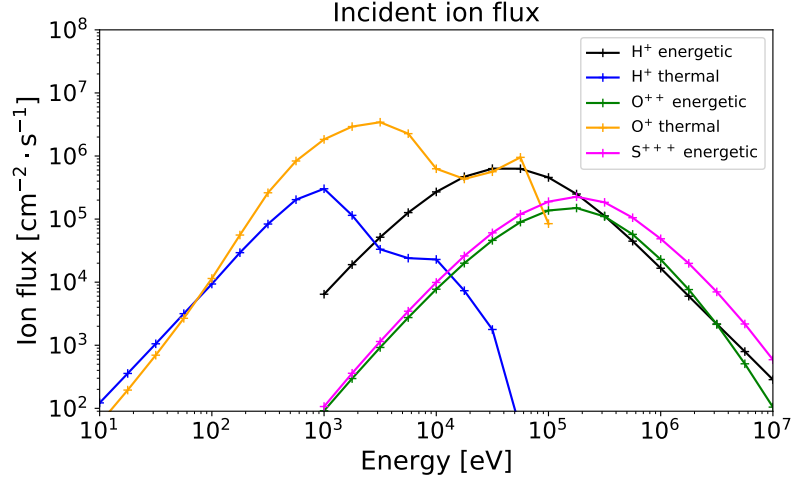


Figure 2. Energy spectra of the precipitating ions used as our input ion populations, integrated over all incident angles and averaged over the surface of Ganymede.

2.2 Sputtering yield

Ion sputtering on water ice has been extensively studied via laboratory experiments and the sputtered products are known to be comprised of H_2O , H_2 , and O_2 (Johnson et al., 2004; Galli et al., 2017). While H_2O is a surface constituent directly sputtered by the impact of ions on water ice, H_2 and O_2 are radiolytic products generated in the material by the irradiation of water ice and subsequently sputtered by projectiles (Johnson et al., 2003; Paranicas et al., 2009; Teolis et al., 2017). Here we use three different functions to calculate the sputtering yield, depending on the energy of the incident and the sputtered species. Throughout the paper, the sputtering yield of a sputtered species by an incident species refers to the number of particles of the sputtered species released from the surface by one incident ion.

At incident ion energies higher than 100 keV, we use the model described in Johnson et al. (2004) to calculate $Y_{\text{H}_2\text{O},high}$, the yield of H_2O as a function of the energy and species of the incident ion:

$$\frac{1}{Y_{\text{H}_2\text{O},high}(v, Z)} = \frac{1}{11.2 Z^{2.8} (v/Z^{1/3})^{-2.24}} + \frac{1}{4.2 Z^{2.8} (v/Z^{1/3})^{2.16}}, \quad (1)$$

where Z is the atomic number of the incident particle and v the velocity of the incident particle in atomic units ($1 \text{ au} = 2.18 \cdot 10^8 \text{ cm} \cdot \text{s}^{-1}$).

At incident ion energies lower than 100 keV, we use the model described in Fam et al. (2008) to calculate $Y_{\text{H}_2\text{O},low}$, the yield of H_2O as a function of the energy, species, and incident angle of the incident particle:

$$Y_{\text{H}_2\text{O},low}(E, m, Z, \beta) = \frac{1}{U_0} \left(\frac{3}{4\pi^2 C_0 \alpha S_n} + \eta S_e^2 \right) \cos^{-f}(\beta), \quad (2)$$

where E , m , and Z are respectively the energy, mass, and atomic number of the projectile. β is the incidence angle, defined from the surface normal. U_0 , C_0 , α , S_n , η , S_e and f are constants; details can be found in Fam et al. (2008).

In eq. 2 we do not include the temperature-dependent component of Famá's model, as it is attributed to H_2 and O_2 produced by radiolysis, a temperature-dependent process. Instead, we calculate the yield of H_2 ($Y_{\text{H}_2}(E, T, \beta)$) and that of O_2 ($Y_{\text{O}_2}(E, T, \beta)$)

153 using the model derived by Teolis et al. (2017):

$$Y_{O_2}(E, T, \beta) = \frac{Y_{H_2}(E, T, \beta)}{2} = \epsilon g_{O_2}^0 x_o \left[1 - \exp\left(-\frac{r_o \cos(\beta)}{x_o}\right) \right] \left[1 + q_o \exp\left(-\frac{Q}{k_b T}\right) \right] / r_o \cos(\beta), \quad (3)$$

154 where T is the temperature of the surface of Ganymede, β the incidence angle of the pro-
 155 jectile measured from the surface normal, and k_b is the Boltzmann constant. Details about
 156 ϵ , $g_{O_2}^0$, x_o , r_o , q_o , and Q can be found in Teolis et al. (2017). The temperature model
 157 used in this study was derived by Marconi (2007) based on data from the Galileo space-
 158 craft (Orton et al., 1996). The dayside temperature is given by $T(\lambda) = 70 \cos(\lambda)^{0.75} +$
 159 80 K (where λ is the sub-solar latitude) and the nightside temperature is a constant 80
 160 K.
 161

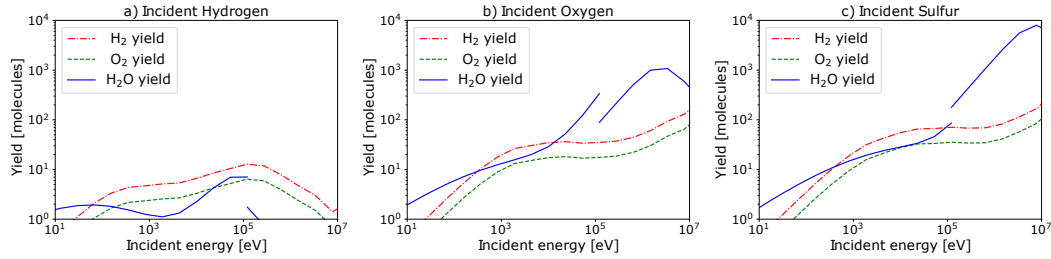


Figure 3. Sputtering yield of H_2O , H_2 and O_2 by incident O, H, and S ions. The discontinuity at 100 keV for the H_2O yields is explained by the transition of the model from Famá’s to Johnson’s. The yields of H_2 and O_2 are calculated using only Teolis’ model.

162 Figure 3 shows the sputtering yield of H_2O , O_2 and H_2 by O, H and S ions imping-
 163 ing on water ice. Generally, the H_2O yield by O and S is higher than 1 and increases with
 164 energy for most of the energy range shown here. Because of its low atomic mass, the yield
 165 by H is much lower. A surface temperature of 124 K was used to generate these figures,
 166 which corresponds to an average daytime disk temperature (Grundy et al., 1999). As
 167 mentioned above, the actual surface temperature used in our model varies between 80
 168 K on the nightside and 150 K at the sub-solar point.

169 2.3 Sputtered energy distribution

170 We assume a Thompson-Sigmund law to calculate the probability distribution $S(K)$
 171 of the energy of the sputtered particles (Sigmund, 1969).

$$172 \quad S(K) \propto \frac{K}{(K + E_b)^3} \cdot \left(1 - \sqrt{\frac{K}{E_b + 4 E_i (M_1 M_2) / (M_1 + M_2)^2}} \right), \quad (4)$$

173 where K is the energy of the sputtered neutral particle, E_b the binding energy of the sur-
 174 face (0.054 eV as also used in Plainaki et al. (2015)), E_i the energy of the projectile, and
 175 M_1 and M_2 are the masses of the projectile and sputtered neutral particle.

176 Figure 4a shows the energy distribution of H_2O molecules sputtered by H, O and
 177 S with an incident energy of 100 keV. The main consequence of the difference in atomic
 178 mass is the cutoff energy of sputtered particles: sputtered H has a cutoff energy of about
 179 20 keV, much lower than the cutoff energy of heavier oxygen and sulfur at about 90 keV.
 180 Figure 4b shows the energy distribution of H_2O , H_2 and O_2 molecules sputtered by 100
 181 keV H. Higher masses result in lower cutoff energies, with respective cutoff energies for
 182 O_2 , H_2O , and H_2 of about 10 keV, 20 keV, and 80 keV.

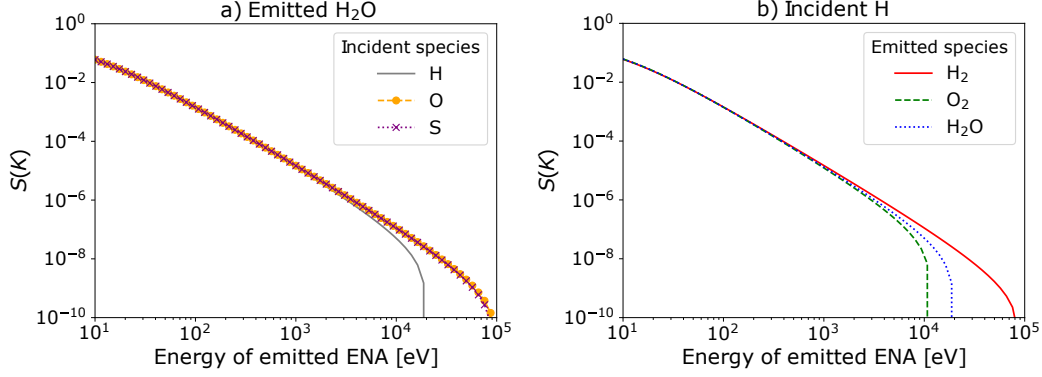


Figure 4. a) Probability distribution of the energy of H₂O sputtered by different incident species. b) Probability distribution of the energy of H₂O, H₂ and O₂ molecules sputtered by H, for incident energies of 100 keV.

183

2.4 Flux calculation

184

The differential flux of the sputtered neutrals, $j(K)$, is calculated from the combination of the above-mentioned parameters, where K is the energy of the sputtered particle. In our model, the incident plasma taken from hybrid simulations is $f(v, \theta, \phi)$, in units of $(\text{m/s})^{-3} \text{sr}^{-1} \text{cm}^{-2} \text{s}^{-1}$, for each bin at the surface (Poppe et al., 2018), where v is the incident velocity, θ the incident elevation, and ϕ the incident azimuth.

186

187

188

The differential flux $j(K)$ (in units $\text{cm}^{-2} \text{s}^{-1} \text{sr}^{-1} \text{eV}^{-1}$) is calculated using the following expression:

189

190

$$j(K) = \frac{1}{2\pi} \int_v \int_\theta \int_\phi f(v, \theta, \phi) Y(E_i) S(K; E_i) v^2 \cos(\alpha) \sin(\theta) dv d\theta d\phi, \quad (5)$$

191

192

193

194

195

196

where E_i the energy of the incident species, $Y(E_i)$ the sputtering yield function, $S(K; E_i)$ the Thompson-Sigmund probability distribution function, and α is the angle between the velocity vector and the local normal vector pointing inward to the center of Ganymede at the corresponding latitude and longitude. We assume that sputtered neutrals are ejected isotropically and therefore divide the flux by 2π to get the flux per solid angle.

197

3 Results

198

3.1 ENA sputtering maps

199

200

201

202

203

204

205

Figure 5 shows the calculated flux maps of the sputtered ENAs (H₂, O₂, and H₂O) integrated over all incident species, incident angles, and energies. The colorbar ranges from 10^6 to $10^{10} \text{ cm}^{-2} \cdot \text{s}^{-1}$ for all three maps. H₂ and O₂ fluxes are about 5 times higher on the dayside than on the nightside due to the higher surface temperature on the dayside, which results in a higher yield of H₂ and O₂ (eq. 3). As the yield of H₂O is independent of temperature, no significant difference between the dayside and the nightside is observed other than that resulting from the input ion precipitation patterns.

206

207

208

209

210

211

Generally, similar patterns to the ion precipitation map (Figure 1) are observed for ENA sputtering. Indeed, the sputtered ENA flux is higher in the polar regions than in the equatorial regions, and the difference in ENA fluxes between the pole and the equator is more distinct in the trailing hemisphere. The similarity between ion precipitation patterns and sputtering rate patterns illustrates the relevance of the ENA imaging method to remotely map ion precipitation at Ganymede, as previously shown for terrestrial bod-

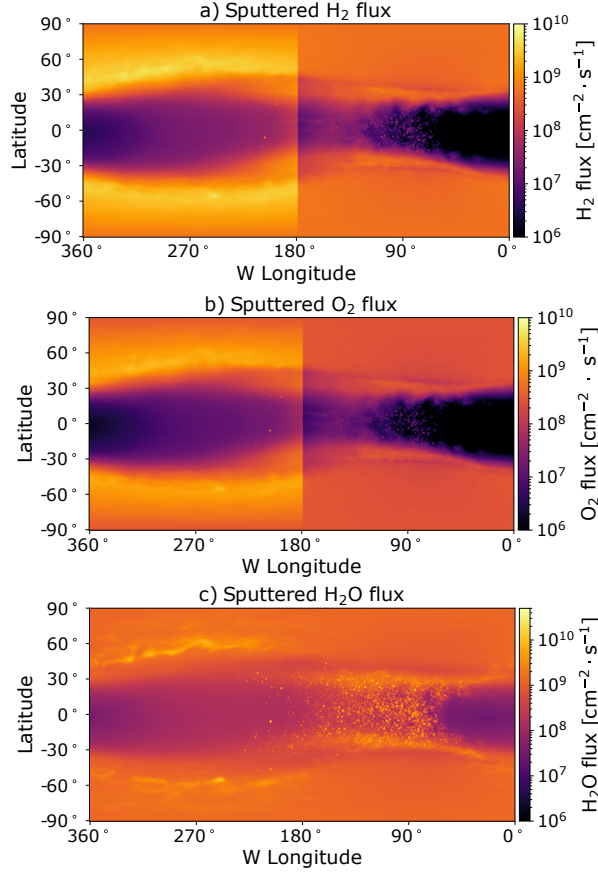


Figure 5. Maps of the sputtered fluxes of H₂, O₂ and H₂O, integrated over all incident species, energies, and angles.

212 ies (Futaana et al., 2006; Vorburger et al., 2014; Wieser et al., 2009; Allegrini et al., 2013;
 213 Futaana et al., 2013).

214 3.2 Sputtered energy distribution

215 Figure 6 shows the energy spectra of sputtered H₂O, H₂, and O₂. Because of the
 216 Thompson-Sigmund law (eq. 4) for the energy of sputtered ENAs, fluxes fall as energy
 217 increases. Although the incident ion population is dominated by the thermal O⁺ com-
 218 ponent at low energies, the contribution of energetic S⁺⁺⁺ ions to the sputtered H₂O,
 219 H₂, and O₂ ENA fluxes dominates over that of all other species across the entire energy
 220 range. This is likely a combined effect of the heavier mass of S⁺⁺⁺ ions, resulting in high
 221 sputtering yields, and the fact that the energy distribution of S⁺⁺⁺ is skewed towards
 222 higher energies.

223 The lowest contribution to sputtered ENAs comes from the thermal H⁺ ion com-
 224 ponent because of their low incident flux (Figure 2) and low sputtering yield, lower than
 225 10 across most of the energy range. For the same reason, energetic H⁺ ions contribute
 226 the least out of the three energetic species to sputtering O₂ and H₂O. Energetic H⁺ ions
 227 sputter less H₂O molecules than thermal O⁺ ions up to 20 keV. At 20 keV, H₂O ENAs
 228 sputtered by O⁺ cut off, due to O⁺ ions being heavier than H⁺ and also contributing
 229 more to the incident ion flux.

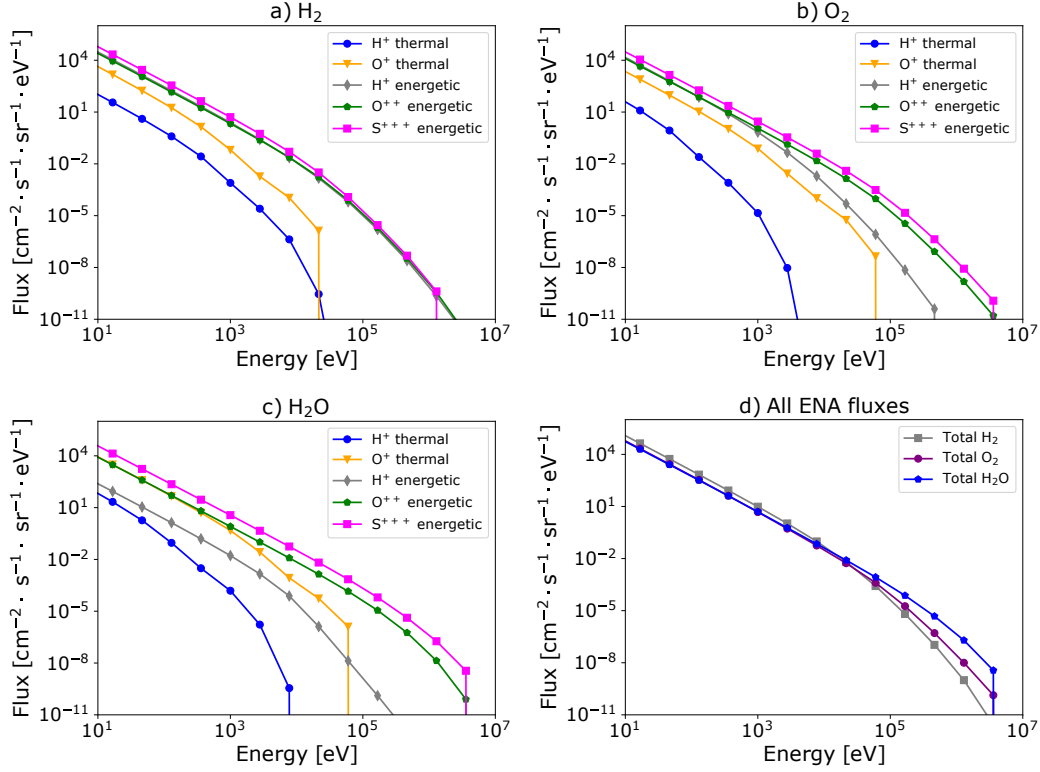


Figure 6. Globally averaged energy distributions of sputtered a) H₂, b) O₂, and c) H₂O, integrated over incident angles and energies. Different colors indicate the incident species which sputtered these ENAs. d) Energy distribution of all sputtered species, summed over incident species.

230 Total sputtered fluxes of H₂O, H₂, and O₂ are compared with one another in Fig-
 231 ure 6d) and are shown to be within the same order of magnitude up to 10 keV. From
 232 10 keV to 4 MeV (where all ENA fluxes cut off), H₂O fluxes dominate over H₂, and O₂.

233 3.3 Total sputtering rate

234 By integrating the sputtered ENA flux over energy and the entire surface we obtain
 235 global sputtering rates of 4.8, 2.4 and 7.0×10^{26} molecules per second for H₂, O₂,
 236 and H₂O respectively. This results in a total sputtering rate of 1.42×10^{27} molecules
 237 per second. Table 1 shows a comparison of our estimated sputtering rate with previous
 238 works. Given from left to right are the model reference, the input plasma model type
 239 (MHD or hybrid), the sputtering model(s), the energy range of the sputtered molecules,
 240 the species of the sputtered molecules, and the total sputtering rate.

241 All works give similar results within two orders of magnitude. The difference be-
 242 tween our result and those of previous works can be qualitatively explained as follows.
 243 Plainaki et al. (2015) derived their ion population using electric and magnetic fields ob-
 244 tained with MHD simulations by Jia et al. (2008). Their energy range covered only 1-
 245 100 keV, which is narrower than in this study, leading to a total sputtering rate one or-
 246 der of magnitude lower than ours. They used Famá's model to calculate the yield of H₂O
 247 and O₂, but did not account for the sputtering of H₂.

248 Poppe et al. (2018), when they published the results of the hybrid simulation of
 249 Jovian plasma which were used in this study, took the opportunity to estimate the H₂O

Table 1. Total sputtering rate from the surface of Ganymede estimated by previously published works as well as this one.

Reference	Input	Sputtering models	Energy range	Sputtered species	Total sputtering rate [s ⁻¹]
Plainaki et al., 2015	MHD ¹	Famá ³	1-100 keV	H ₂ O, O ₂	6.94×10^{25}
Poppe et al., 2018	Hybrid ²	Johnson ⁴	10 eV - 10 MeV	H ₂ O	7.5×10^{26}
Carnielli et al., 2020	MHD ¹	Famá ³ , Johnson ⁴	1 eV - 30 MeV	H ₂ O	2.25×10^{27}
This work	Hybrid ²	Famá ³ , Johnson ⁴ , Teolis ⁵	10 eV - 10 MeV	H ₂ O, O ₂ H ₂	1.42×10^{27}

¹ Jia et al. (2008)² Fatemi et al. (2016)³ Fam et al. (2008)⁴ Johnson et al. (2004)⁵ Teolis et al. (2017)

250 ENA sputtering rate using Johnson’s model. However, at incident energies lower than
 251 100 keV, Johnson’s model underestimates the yield, which is better reproduced by Famá’s
 252 (Cassidy et al., 2013). Moreover, Poppe et al. (2018) considered only the sputtering of
 253 H₂O, whereas we considered O₂ and H₂ in addition to H₂O.

254 Carnielli et al. (2020) used the model in Jia et al. (2008) also used to derive their
 255 input ion population, but considered energies ranging from 1 eV to 30 MeV, a wider en-
 256 ergy range than used here. Moreover, they considered the contribution of Ganymede’s
 257 ionospheric ions, which they showed can contribute to up to 10% of the ENA sputter-
 258 ing rate. Their ionospheric ion population was comprised of O₂⁺, O⁺, H₂O, H₂⁺, H⁺, and
 259 OH⁺ with energies ranging from 10 eV to 10 keV. As our input population did not in-
 260 clude ionospheric ions and covered a narrower energy range, our total sputtering rate is
 261 expected to be lower than theirs.

262 Our results suggest that H₂ and O₂ account for half of the total neutral sputter-
 263 ing rate from the surface of Ganymede, showing that their contribution should be con-
 264 sidered in addition to that of H₂O.

265 3.4 JNA count rate estimation

266 The JUICE spacecraft, planned to launch in 2022 and expected to reach Jupiter
 267 in the 2030s, carries the Particle Environment Package (PEP). PEP is comprised of six
 268 sensors tailored to study how Jovian plasma interacts with Ganymede’s magnetosphere,
 269 tenuous atmosphere, and icy surface. In particular, the Jovian Neutrals Analyzer (JNA)
 270 will measure ENAs in the Jovian environment in the energy range between 10 eV to 3.3
 271 keV, with a field-of-view of 15°×150° divided into 11 pixels (Shimoyama et al., 2018).

272 Here we estimate the count rate that JNA is expected to observe at Ganymede by
 273 multiplying the flux calculated in section 3.2 by JNA’s estimated geometric factor, GF =
 274 10⁻⁵ cm² · sr · eV/eV. Figure 7 shows simulated JNA count rates as a function of en-
 275 ergy. The geometric factor we used is constant across the energy range, so the count rate
 276 distribution follows the Thompson-Sigmund law applied to the sputtered ENAs, result-

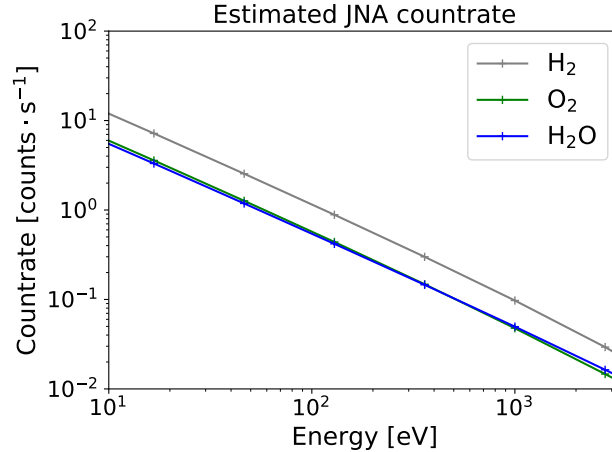


Figure 7. Simulated JNA count rate as a function of energy for sputtered H₂O, O₂ and H₂ in the energy range JNA can measure.

277 ing in count rates as high as 10^1 counts·s⁻¹ at 20 eV and as low as 10^{-2} counts·s⁻¹
 278 at 3.3 keV. JNA is optimized to measure small fluxes, i.e. low count rates, even in the
 279 harsh radiation environment expected at Jupiter. However, such a spectra indicates that
 280 longer integration times are needed at high energies than at low energies, an important
 281 consideration for operations planning and future data analysis. As we did not account
 282 for any dissociative processes of the sputtered ENAs, we assume here that H₂, O₂, and
 283 H₂O are observed and detected by JNA as molecules. In reality, any molecule entering
 284 JNA would most likely be dissociated upon encountering JNA’s conversion surface, as
 285 JNA uses a charge conversion surface to ionize ENAs in order to analyze their energy
 286 and guide them to JNA’s detectors (Kazama et al., 2007). Since dissociated products
 287 would each leave the conversion surface with less energy than the original molecule, the
 288 assumption that JNA observes molecules likely gives an underestimation of the count
 289 rate JNA would measure at low energies.

290 3.5 JNA simulated observation

291 To illustrate JNA’s ability to measure the variability of Jovian plasma precipita-
 292 tion at Ganymede, we calculate the differential ion flux at different latitudes on Ganymede.
 293 In Figure 8, the JUICE spacecraft is assumed to orbit Ganymede at an altitude of 1000km
 294 along the 90°W and 270°W meridians. At four locations along the orbital track, the flux
 295 was averaged over areas corresponding to the size of the footprint of JNA’s center pixel.
 296 Those areas are referred to as zones. For each zone, the fluxes of sputtered H₂, O₂, and
 297 H₂O are shown, as well as the JNA one count level.

298 Zone 1 is situated at Ganymede’s north pole and covers areas on both the dayside
 299 and the nightside. Zone 2 is centered around the sub-solar point. Zone 3 is located along
 300 the sub-solar longitude at latitude 60°N, near the open-closed field-line boundary where
 301 the ion flux peaks. Zone 4 is centered around the anti-solar point on the nightside.

302 Figure 8c shows that the highest flux is observed in Zone 3, reflecting the peak in
 303 ion flux at this location near the open-closed field-line boundary where both energetic
 304 and thermal plasma have easy access to the surface. The ion population there is domi-
 305 nated by thermal O⁺ (see Poppe et al. (2018) for incident ion flux distributions at dif-
 306 ferent regions on Ganymede). Zone 1, over the north pole, is exposed to an ion popu-
 307 lation similar to that in Zone 3, although precipitation at the poles is less intense. Con-

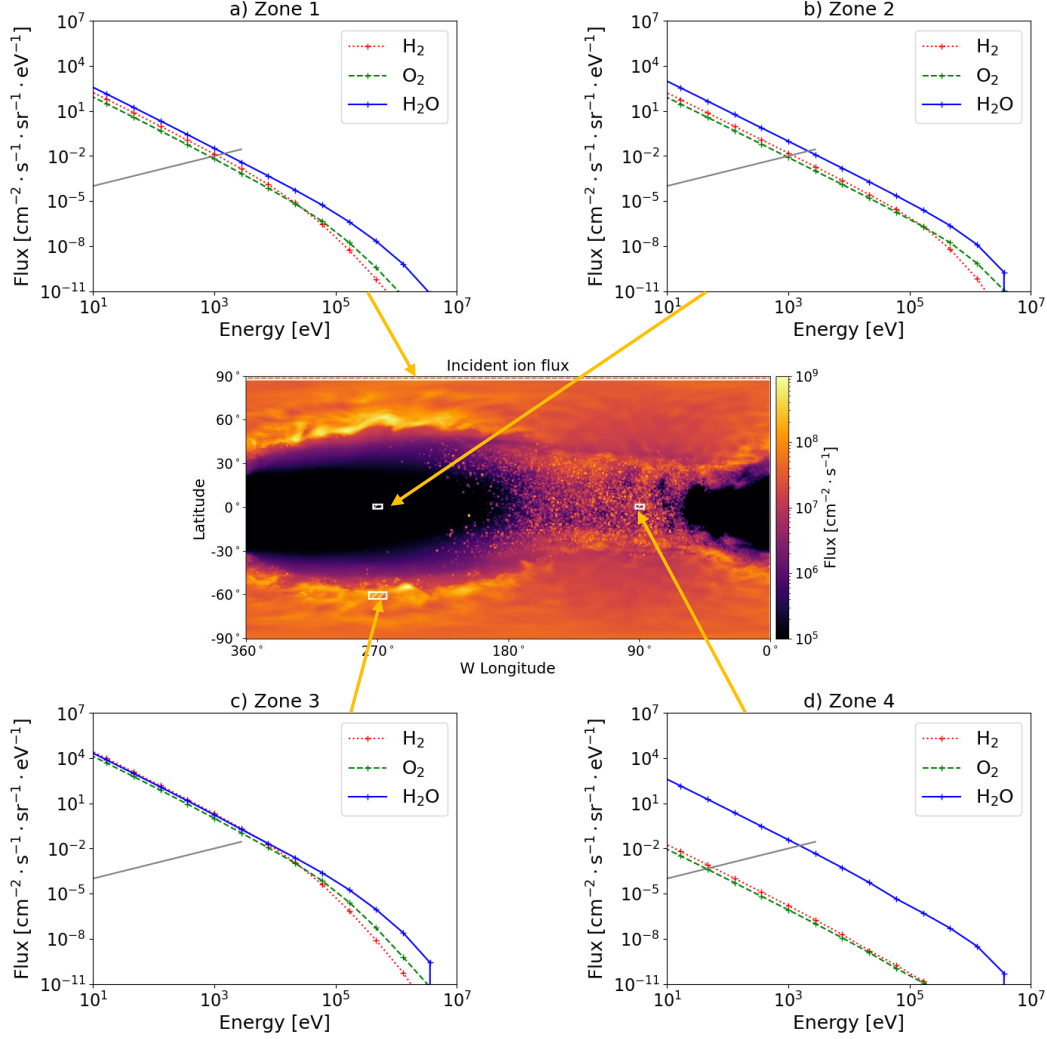


Figure 8. Flux of sputtered H_2 , O_2 and H_2O at four locations on the surface of Ganymede, integrated over incident angles and energies. White rectangles show the area over which the flux was averaged and correspond to the footprint of JNA at 1000 km above the surface of Ganymede. The solid gray line indicates the one count level of the JNA instrument for the energy range that JNA can measure (10 eV to 3.3 keV).

308 subsequently, the ENA flux is lower in Zone 1. Zone 2 is centered around the sub-solar point,
 309 where the incident ion flux is three orders of magnitude lower than in Zone 3, as Ganymede's
 310 magnetic field prevents low energy Jovian plasma from accessing the surface. The ion
 311 flux in Zone 2 is therefore dominated by energetic species, which are more efficient at
 312 sputtering H_2O than H_2 and O_2 (see Figure 3). This explains why the sputtered H_2O
 313 flux is about one order higher than that of H_2 and O_2 . Figure 8d shows an even larger
 314 gap between H_2O fluxes and H_2 and O_2 fluxes but there the cause is different. In Zone
 315 4, the ion flux includes contributions of both thermal and energetic species. However,
 316 Zone 4 is located on the nightside where the surface temperature is 80 K, which leads
 317 to much lower sputtering yields for H_2 and O_2 than for H_2O .

318 As sputtered fluxes of H_2O are not temperature-dependent, their variation is a direct
 319 result of the differences between the incident sputtering populations. We plot them

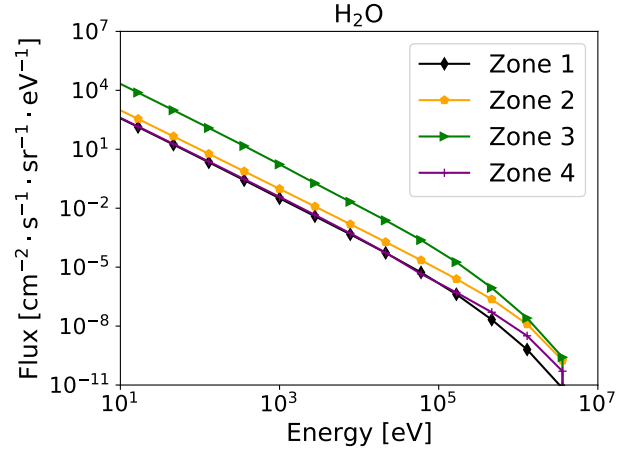


Figure 9. Sputtered H₂O fluxes for all zones, integrated over incident species, energies, and angles.

320 together in Figure 9 for easier comparison. The intense ion flux in Zone 3 yields the highest
 321 sputtered H₂O flux at all energies. Despite their different incident ion populations,
 322 Zone 1 and Zone 4 shows similar sputtered H₂O fluxes, up to 100 keV, above which ener-
 323 getic ions in Zone 4 result in a higher sputtered H₂O flux. While the incident ion flux
 324 is lowest in Zone 2, the sputtered H₂O flux is higher than in Zone 1 and 4, for the rea-
 325 sons mentioned above.

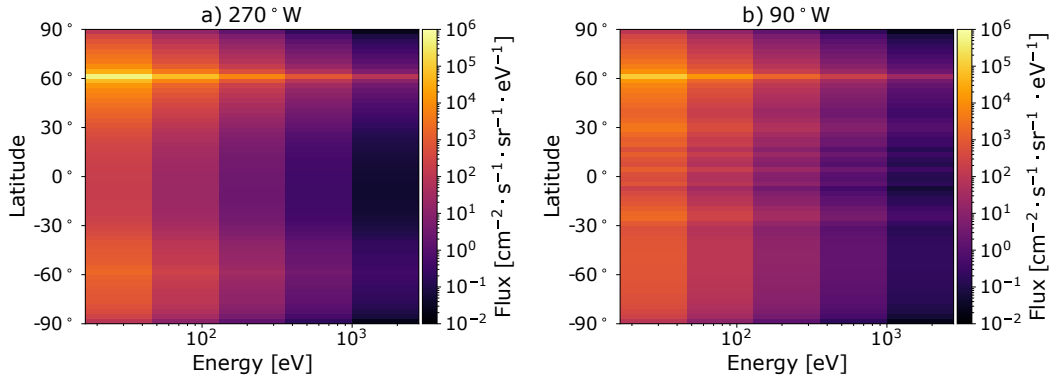


Figure 10. Flux of sputtered ENAs integrated over sputtered species and incident species, angles, and energies, shown for each latitude zone corresponding to a JNA footprint along a) 270°W and b) 90°W.

326 In Figure 10, JNA is also assumed to orbit Ganymede at 1000km along the 90°W
 327 and 270°W meridians but here we divide the orbit track into 120 zones covering 3° each
 328 in latitude (corresponding to the width of JNA’s center pixel in elevation). The flux for
 329 each latitude zone is shown, for the energy range that JNA can measure (between 10 eV
 330 and 3.3 keV) and integrated over sputtered species and incident species, angles, and en-
 331 ergies.

332 Generally, Figure 10 shows that the flux of sputtered ENAs varies by about four
 333 orders of magnitude along the simulated trajectory of JNA for all energy bins in the JNA

334 measuring range. Again we observe that the variability of the sputtered neutral flux re-
 335 flects that of the incident ion flux. Along the 270°W meridian (on the dayside/trailing
 336 hemisphere), the flux gradually decreases from latitudes $\pm 60^\circ$ to the equator where the
 337 flux is minimal and four orders of magnitude lower than at $+60^\circ$. We do note that while
 338 the results from Poppe’s backwards-Liouville tracing model show a significantly higher
 339 flux at $+60^\circ$ than at -60° for the G8 flyby, a significant difference between the north-
 340 ern and southern hemispheres is not expected in reality.

341 On the 90°W meridian (on the nightside/leading hemisphere), the gradual decrease
 342 is interrupted at latitudes $\pm 30^\circ$ by narrow bands of intense sputtering, reflecting the nar-
 343 row bands of intense ion precipitation in the incident flux (Figure 1). At these latitudes,
 344 the relative variation between adjacent zones is a factor of two to three. These large lat-
 345 itudinal variations show that ion precipitation patterns at the surface of Ganymede can
 346 be retrieved by remotely measuring ENAs.

347 4 Discussion and Conclusions

348 We presented a new method to simulate the sputtering process at Ganymede, in
 349 order to estimate sputtered ENA fluxes to be observed by the Jovian Neutrals Analyzer,
 350 an ENA sensor to be deployed at Ganymede by ESA’s upcoming JUICE mission. Our
 351 method combines three sputtering yield models to calculate the yield of H_2 , O_2 , and H_2O
 352 separately. Our global sputtering rates show that H_2 and O_2 account for half of the to-
 353 tal global sputtering rate from Ganymede. Our total global sputtering rate is in agree-
 354 ment with previous works, but by separating each species we were able to calculate their
 355 energy spectra, which is necessary in order to simulate JNA measurements. Indeed, JNA’s
 356 mass resolution only allows it to distinguish between H and heavier species, but infor-
 357 mation about the mass and origin of heavier species may be retrieved by looking at their
 358 energy spectra. In this study we used a Thompson-Sigmund law to calculate the energy
 359 spectra of sputtered particles. In future work, the backscattering process should also be
 360 considered to more accurately simulate the energy spectra of ENAs to be observed at
 361 Ganymede. Backscattering is another process caused by precipitating ions, in which the
 362 impinging ion is neutralized (usually) and reflected by the surface. Measurements both
 363 in laboratories and in space suggest that backscattered particles would have energies in
 364 the range that JNA can measure, but distributed according to a Maxwell-Boltzmann-
 365 like law rather than the Thompson-Sigmund law applicable to sputtering (Futaana et
 366 al., 2012; Wieser et al., 2016). Backscattering yields are not well modeled, although stud-
 367 ies by Wieser et al. (2016) and Futaana et al. (2012) suggest that a yield of about 0.1-
 368 0.2 can be applied for low (\sim keV) energies. The majority of ENAs in the 10 eV - 1 keV
 369 range are produced by the sputtering process (by high energy particles), so the backscat-
 370 tered contribution to the total ENA spectra is expected to be small. Nevertheless, the
 371 different shape of their spectra may allow us to distinguish backscattered ENAs from sput-
 372 tered ENAs.

373 We also provided an estimate of expected JNA count rates and simulated the sput-
 374 tered ENA flux at different locations along the track of a simplified orbit of the JUICE
 375 spacecraft. Our results show large latitudinal variations in sputtered ENA flux, demon-
 376 strating that JNA will be able to identify ion precipitation patterns by measuring ENAs.
 377 Future work will use realistic orbits of the JUICE spacecraft as well as JNA’s calibrated
 378 instrument response, unavailable at the time of this study.

379 In conclusion, our results provide insight into the appearance of the data when JNA
 380 measures ENAs at Ganymede, as well as how the instrument should be operated opti-
 381 mally under limited power and data budget. The produced sputtering rate maps, energy
 382 spectra, and count rates in this study illustrate the capability of the ENA measuring tech-
 383 nique to remotely map ion precipitation at Ganymede and provide clues for further po-
 384 tential ENA mapping in other icy bodies. Future work can easily use our model to pro-

385 duce more accurately simulated JNA spectra for different phases of the JUICE mission.
 386 Such simulations are crucial for optimizing operations planning and make the most of
 387 the limited integration time and data budget.

388 Acronyms

389 **ENA** Energetic Neutral Atoms
 390 **ESA** European Space Agency
 391 **JNA** Jovian Neutrals Analyzer
 392 **JUICE** JUpiter ICy Moon Explorer
 393 **PEP** Particle Environment Package

394 Acknowledgments

395 A.P. acknowledges support from the Swedish National Space Agency, grant 189/16. S.F.
 396 acknowledges support from the Swedish National Space Agency, grant 179/18. A.R.P.
 397 acknowledges support from NASA SSW grant #NNX16AR99G. Model results for this
 398 work are in the process of being archived at data.irf.se (institutional repository of the
 399 corresponding author).

400 References

- 401 Allegrini, F., Dayeh, M. A., Desai, M. I., Funsten, H. O., Fuselier, S. A., Janzen,
 402 P. H., . . . Wurz, P. (2013, September). Lunar energetic neutral atom (ENA)
 403 spectra measured by the interstellar boundary explorer (IBEX). *Planetary and*
 404 *Space Science*, *85*, 232–242. doi: 10.1016/j.pss.2013.06.014
- 405 Baragiola, R., Vidal, R., Svendsen, W., Schou, J., Shi, M., Bahr, D., & Atteberry,
 406 C. (2003, August). Sputtering of water ice. *Nuclear Instruments and Methods*
 407 *in Physics Research Section B: Beam Interactions with Materials and Atoms*,
 408 *209*, 294–303. doi: 10.1016/S0168-583X(02)02052-9
- 409 Carnielli, G., Galand, M., Leblanc, F., Modolo, R., Beth, A., & Jia, X. (2020,
 410 November). Simulations of ion sputtering at Ganymede. *Icarus*, *351*, 113918.
 411 doi: 10.1016/j.icarus.2020.113918
- 412 Cassidy, T., Coll, P., Raulin, F., Carlson, R. W., Johnson, R. E., Loeffler, M. J.,
 413 . . . Baragiola, R. A. (2010, June). Radiolysis and Photolysis of Icy Satellite
 414 Surfaces: Experiments and Theory. *Space Science Reviews*, *153*(1-4), 299–315.
 415 doi: 10.1007/s11214-009-9625-3
- 416 Cassidy, T., Paranicas, C., Shirley, J., Dalton III, J., Teolis, B., Johnson, R., . . .
 417 Hendrix, A. (2013, March). Magnetospheric ion sputtering and water
 418 ice grain size at Europa. *Planetary and Space Science*, *77*, 64–73. doi:
 419 10.1016/j.pss.2012.07.008
- 420 Cooper, J. (2001, January). Energetic Ion and Electron Irradiation of the Icy
 421 Galilean Satellites. *Icarus*, *149*(1), 133–159. doi: 10.1006/icar.2000.6498
- 422 Fam, M., Shi, J., & Baragiola, R. (2008, January). Sputtering of ice by low-energy
 423 ions. *Surface Science*, *602*(1), 156–161. doi: 10.1016/j.susc.2007.10.002
- 424 Fatemi, S., Poppe, A. R., Khurana, K. K., Holmström, M., & Delory, G. T. (2016).
 425 On the formation of Ganymede’s surface brightness asymmetries: Kinetic sim-
 426 ulations of Ganymede’s magnetosphere. *Geophysical Research Letters*, *43*(10),
 427 4745–4754. doi: 10.1002/2016GL068363
- 428 Futaana, Y., Barabash, S., Grigoriev, A., Winningham, D., Frahm, R., Ya-
 429 mauchi, M., & Lundin, R. (2006, October). Global Response of Mar-
 430 tian Plasma Environment to an Interplanetary Structure: From Ena and
 431 Plasma Observations at Mars. *Space Science Reviews*, *126*(1), 315–332. doi:

- 432 10.1007/s11214-006-9026-9
- 433 Futaana, Y., Barabash, S., Wieser, M., Holmström, M., Lue, C., Wurz, P., . . .
 434 Asamura, K. (2012, May). Empirical energy spectra of neutralized solar
 435 wind protons from the lunar regolith: EMPIRICAL MODEL OF BACKSCAT-
 436 TERED ENA. *Journal of Geophysical Research: Planets*, *117*(E5), n/a–n/a.
 437 doi: 10.1029/2011JE004019
- 438 Futaana, Y., Barabash, S., Wieser, M., Lue, C., Wurz, P., Vorbürger, A., . . .
 439 Asamura, K. (2013). Remote energetic neutral atom imaging of electric
 440 potential over a lunar magnetic anomaly. *Geophysical Research Letters*, *40*(2),
 441 262–266. doi: 10.1002/grl.50135
- 442 Galli, A., Vorbürger, A., Wurz, P., Cerubini, R., & Tulej, M. (2018, September).
 443 First experimental data of sulphur ions sputtering water ice. *Icarus*, *312*, 1–6.
 444 doi: 10.1016/j.icarus.2018.04.029
- 445 Galli, A., Vorbürger, A., Wurz, P., & Tulej, M. (2017, July). Sputtering of wa-
 446 ter ice films: A re-assessment with singly and doubly charged oxygen and
 447 argon ions, molecular oxygen, and electrons. *Icarus*, *291*, 36–45. doi:
 448 10.1016/j.icarus.2017.03.018
- 449 Grundy, W. M., Buie, M. W., Stansberry, J. A., Spencer, J. R., & Schmitt, B.
 450 (1999). Near-infrared spectra of icy outer solar system surfaces: Remote
 451 determination of H₂O ice temperatures. *Icarus*, *142*(2), 536–549.
- 452 Gruntman, M. (1997, October). Energetic neutral atom imaging of space plasmas.
 453 *Review of Scientific Instruments*, *68*(10), 3617–3656. doi: 10.1063/1.1148389
- 454 Jia, X., Walker, R. J., Kivelson, M. G., Khurana, K. K., & Linker, J. A. (2008,
 455 June). Three-dimensional MHD simulations of Ganymede’s magnetosphere:
 456 GANYMEDE MHD SIMULATION. *Journal of Geophysical Research: Space
 457 Physics*, *113*(A6), n/a–n/a. doi: 10.1029/2007JA012748
- 458 Johnson, R. E. (1990). *Energetic Charged-Particle Interactions with Atmospheres
 459 and Surfaces*. Berlin Heidelberg: Springer-Verlag. doi: 10.1007/978-3-642
 460 -48375-2
- 461 Johnson, R. E., Carlson, R. W., Cooper, J. F., Paranicas, C., Moore, M. H., &
 462 Wong, M. C. (2004). Radiation effects on the surfaces of the Galilean satel-
 463 lites. *Jupiter: The planet, satellites and magnetosphere*, 485–512.
- 464 Johnson, R. E., Quickenden, T. I., Cooper, P. D., McKinley, A. J., & Freeman,
 465 C. G. (2003, December). The Production of Oxidants in Europa’s Surface.
 466 *Astrobiology*, *3*(4), 823–850. (Publisher: Mary Ann Liebert, Inc., publishers)
 467 doi: 10.1089/153110703322736123
- 468 Kazama, Y., Barabash, S., Wieser, M., Asamura, K., & Wurz, P. (2007, Septem-
 469 ber). Development of an LENA instrument for planetary missions by nu-
 470 merical simulations. *Planetary and Space Science*, *55*(11), 1518–1529. doi:
 471 10.1016/j.pss.2006.11.027
- 472 Khurana, K., Pappalardo, R., Murphy, N., & Denk, T. (2007, November). The origin
 473 of Ganymede’s polar caps. *Icarus*, *191*(1), 193–202. doi: 10.1016/j.icarus.2007
 474 .04.022
- 475 Leblanc, F., Oza, A. V., Leclercq, L., Schmidt, C., Cassidy, T., Modolo, R.,
 476 . . . Johnson, R. E. (2017, September). On the orbital variability of
 477 Ganymede’s atmosphere. *Icarus*, *293*, 185–198. (arXiv: 1804.10592) doi:
 478 10.1016/j.icarus.2017.04.025
- 479 Marconi, M. (2007, September). A kinetic model of Ganymede’s atmosphere. *Icarus*,
 480 *190*(1), 155–174. doi: 10.1016/j.icarus.2007.02.016
- 481 McComas, D. J., Allegrini, F., Bochsler, P., Frisch, P., Funsten, H. O., Grunt-
 482 man, M., . . . Schwadron, N. A. (2009). Lunar backscatter and
 483 neutralization of the solar wind: First observations of neutral atoms
 484 from the Moon. *Geophysical Research Letters*, *36*(12). (eprint:
 485 <https://agupubs.onlinelibrary.wiley.com/doi/pdf/10.1029/2009GL038794>)
 486 doi: <https://doi.org/10.1029/2009GL038794>

- 487 Orton, G. S., Spencer, J. R., Travis, L. D., Martin, T. Z., & Tamppari, L. K. (1996,
488 October). Galileo Photopolarimeter-Radiometer Observations of Jupiter and
489 the Galilean Satellites. *Science*, *274*(5286), 389–391. (Publisher: American
490 Association for the Advancement of Science Section: Reports) doi: 10.1126/
491 science.274.5286.389
- 492 Paranicas, C., Cooper, J. F., Garrett, H. B., Johnson, R. E., & Sturmer, S. J. (2009).
493 Europa’s Radiation Environment and Its Effects on the Surface. *Europa*,
494 Edited by Robert T. Pappalardo, William B. McKinnon, Krishan K. Khurana ;
495 with the assistance of Ren Dotson with 85 collaborating authors. University of
496 Arizona Press, Tucson, 2009. The University of Arizona space science series
497 ISBN: 9780816528448, p.529, 529.
- 498 Plainaki, C., Massetti, S., Jia, X., Mura, A., Milillo, A., Grassi, D., . . . Filacchione,
499 G. (2020, September). Kinetic Simulations of the Jovian Energetic Ion Circu-
500 lation around Ganymede. *The Astrophysical Journal*, *900*(1), 74. (Publisher:
501 American Astronomical Society) doi: 10.3847/1538-4357/aba94c
- 502 Plainaki, C., Milillo, A., Massetti, S., Mura, A., Jia, X., Orsini, S., . . . Rispoli, R.
503 (2015, January). The H₂O and O₂ exospheres of Ganymede: The result of a
504 complex interaction between the jovian magnetospheric ions and the icy moon.
505 *Icarus*, *245*, 306–319. doi: 10.1016/j.icarus.2014.09.018
- 506 Plainaki, C., Milillo, A., Mura, A., Orsini, S., & Cassidy, T. (2010, November). Neu-
507 tral particle release from Europas surface. *Icarus*, *210*(1), 385–395. doi: 10
508 .1016/j.icarus.2010.06.041
- 509 Plainaki, C., Milillo, A., Mura, A., Orsini, S., Massetti, S., & Cassidy, T. (2012,
510 April). The role of sputtering and radiolysis in the generation of Europa exo-
511 sphere. *Icarus*, *218*(2), 956–966. doi: 10.1016/j.icarus.2012.01.023
- 512 Poppe, A. R., Fatemi, S., & Khurana, K. K. (2018, June). Thermal and Energetic
513 Ion Dynamics in Ganymede’s Magnetosphere. *Journal of Geophysical Research:*
514 *Space Physics*, *123*(6), 4614–4637. doi: 10.1029/2018JA025312
- 515 Shematovich, V. I. (2016, July). Neutral atmosphere near the icy surface of
516 Jupiters moon Ganymede. *Solar System Research*, *50*(4), 262–280. doi:
517 10.1134/S0038094616040067
- 518 Shimoyama, Asamura, K., Pontoni, A., Neuland, M. B., Karlsson, S., Wieser, M., . . .
519 Barabash, S. (2018). Jovian Neutrals Analyzer for the Particle Environment
520 Package onboard JUICE. , 2.
- 521 Sigmund, P. (1969). Theory of sputtering. I. Sputtering yield of amorphous and
522 polycrystalline targets. *Physical review*, *184*(2), 383.
- 523 Siscoe, G. L., Eviatar, A., Thorne, R. M., Richardson, J. D., Bagenal, F., & Sulli-
524 van, J. D. (1981). Ring current impoundment of the Io plasma torus. *Jour-*
525 *nal of Geophysical Research: Space Physics*, *86*(A10), 8480–8484. (_eprint:
526 <https://agupubs.onlinelibrary.wiley.com/doi/pdf/10.1029/JA086iA10p08480>)
527 doi: <https://doi.org/10.1029/JA086iA10p08480>
- 528 Siscoe, G. L., & Summers, D. (1981). Centrifugally driven
529 diffusion of iogenic plasma. *Journal of Geophysical Re-*
530 *search: Space Physics*, *86*(A10), 8471–8479. (_eprint:
531 <https://agupubs.onlinelibrary.wiley.com/doi/pdf/10.1029/JA086iA10p08471>)
532 doi: <https://doi.org/10.1029/JA086iA10p08471>
- 533 Teolis, B. D., Plainaki, C., Cassidy, T. A., & Raut, U. (2017, October). Water Ice
534 Radiolytic O₂, H₂, and H₂O₂ Yields for Any Projectile Species, Energy, or
535 Temperature: A Model for Icy Astrophysical Bodies. *Journal of Geophysical*
536 *Research: Planets*, *122*(10), 1996–2012. doi: 10.1002/2017JE005285
- 537 Turc, L., Leclercq, L., Leblanc, F., Modolo, R., & Chaufray, J.-Y. (2014, February).
538 Modelling Ganymedes neutral environment: A 3D test-particle simulation.
539 *Icarus*, *229*, 157–169. doi: 10.1016/j.icarus.2013.11.005
- 540 Vorburget, A. (2018). Europa’s ice-related atmosphere: The sputter contribution.
541 Vorburget, A., Wurz, P., Barabash, S., Wieser, M., Futaana, Y., Holmstrm, M.,

- 542 ... Asamura, K. (2014). First direct observation of sputtered lunar oxygen.
543 *Journal of Geophysical Research: Space Physics*, *119*(2), 709–722. (eprint:
544 <https://agupubs.onlinelibrary.wiley.com/doi/pdf/10.1002/2013JA019207>) doi:
545 <https://doi.org/10.1002/2013JA019207>
- 546 Wieser, M., Barabash, S., Futaana, Y., Holmström, M., Bhardwaj, A., Sridharan, R.,
547 ... Asamura, K. (2009, December). Extremely high reflection of solar wind
548 protons as neutral hydrogen atoms from regolith in space. *Planetary and Space*
549 *Science*, *57*(14-15), 2132–2134. doi: 10.1016/j.pss.2009.09.012
- 550 Wieser, M., Futaana, Y., Barabash, S., & Wurz, P. (2016, May). Emission of en-
551 ergetic neutral atoms from water ice under Ganymede surface-like conditions.
552 *Icarus*, *269*, 91–97. doi: 10.1016/j.icarus.2015.12.043
- 553 Wurz, P., Whitby, J., Rohner, U., Martín-Fernández, J., Lammer, H., & Kolb, C.
554 (2010, October). Self-consistent modelling of Mercurys exosphere by sputter-
555 ing, micro-meteorite impact and photon-stimulated desorption. *Planetary and*
556 *Space Science*, *58*(12), 1599–1616. doi: 10.1016/j.pss.2010.08.003

Figure 1.

Incident ion flux

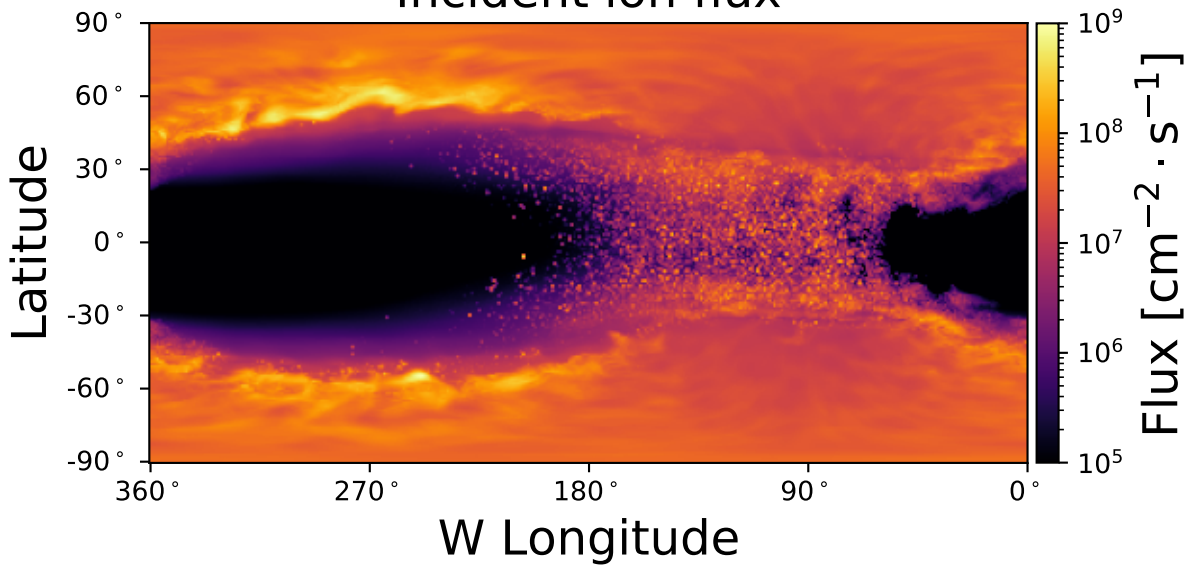


Figure 2.

Incident ion flux

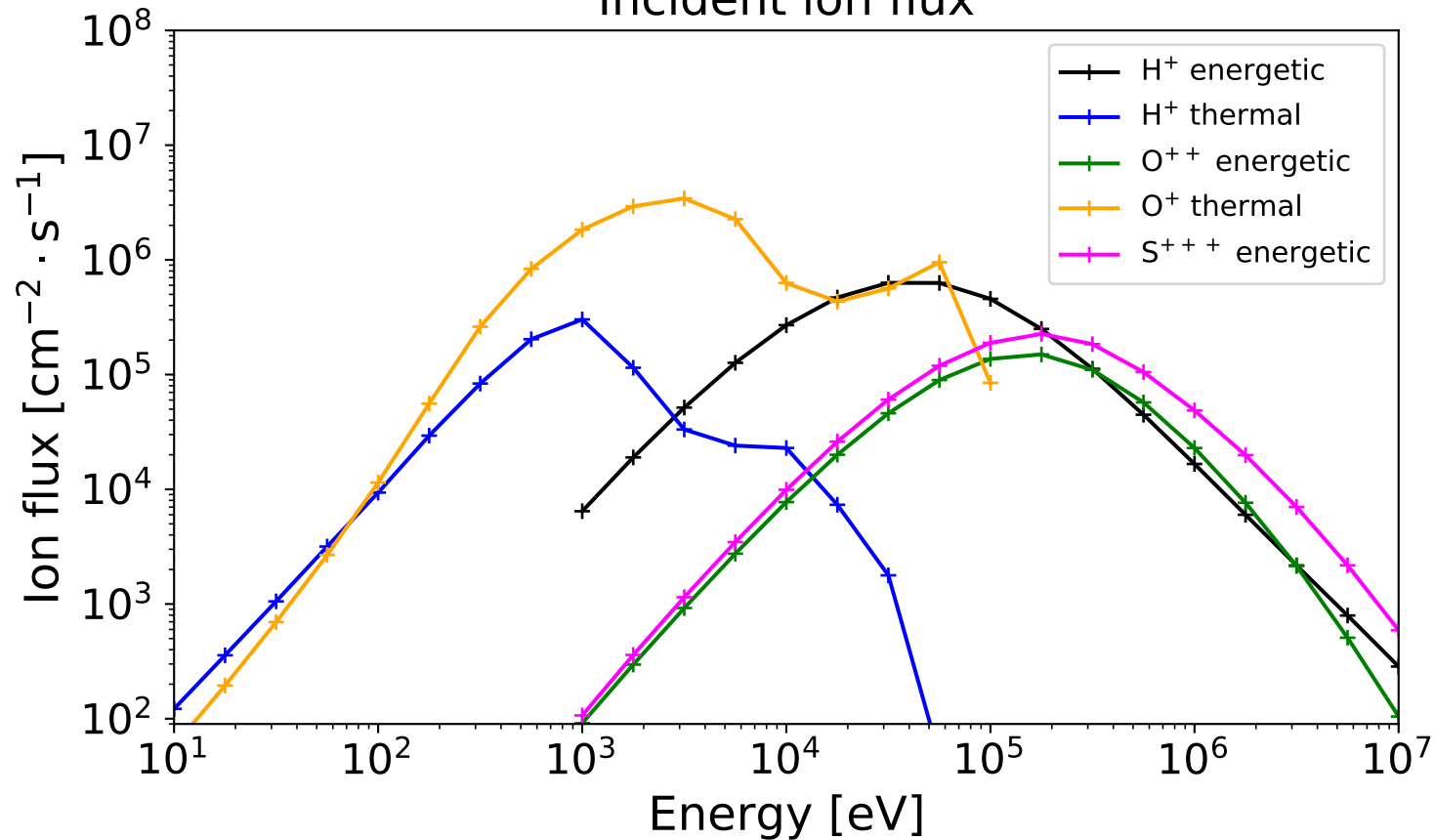


Figure 3.

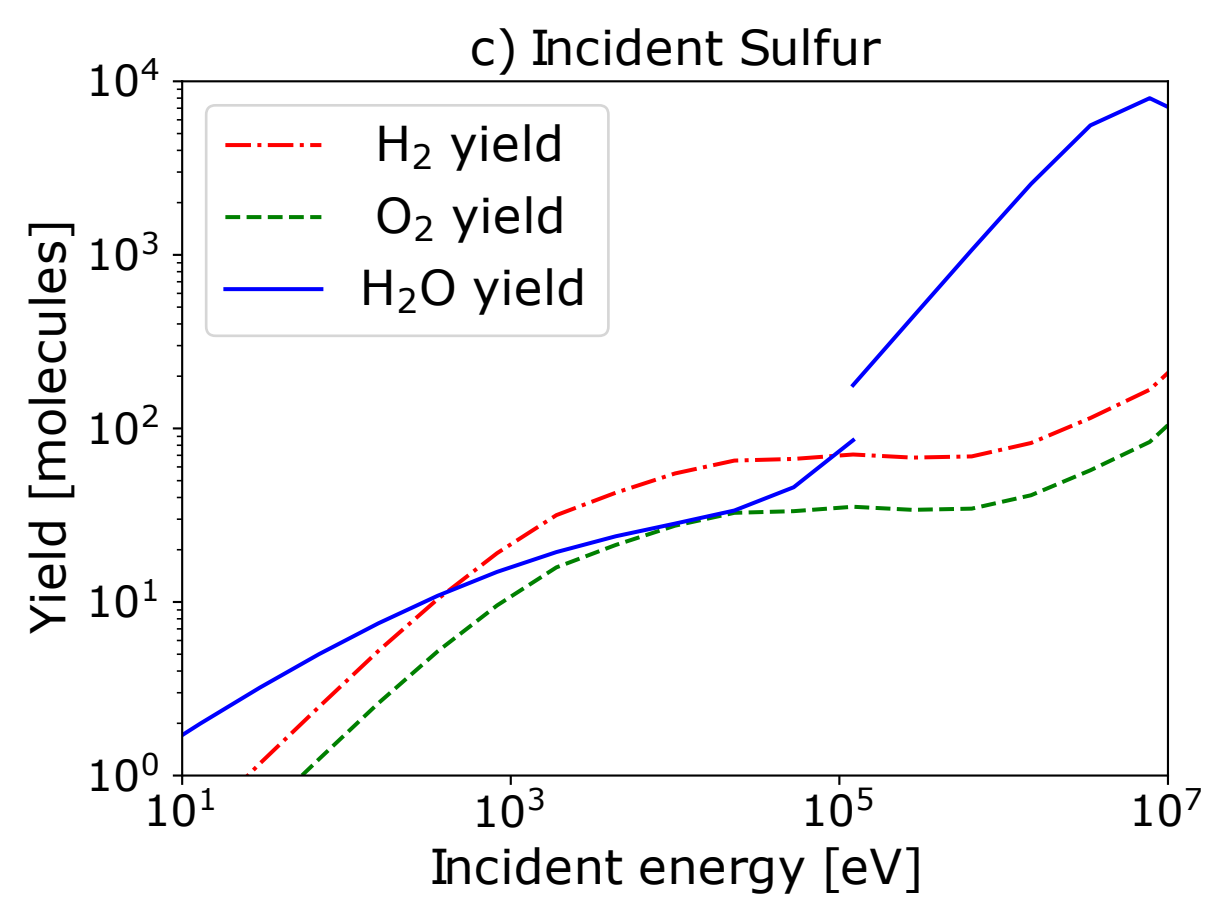
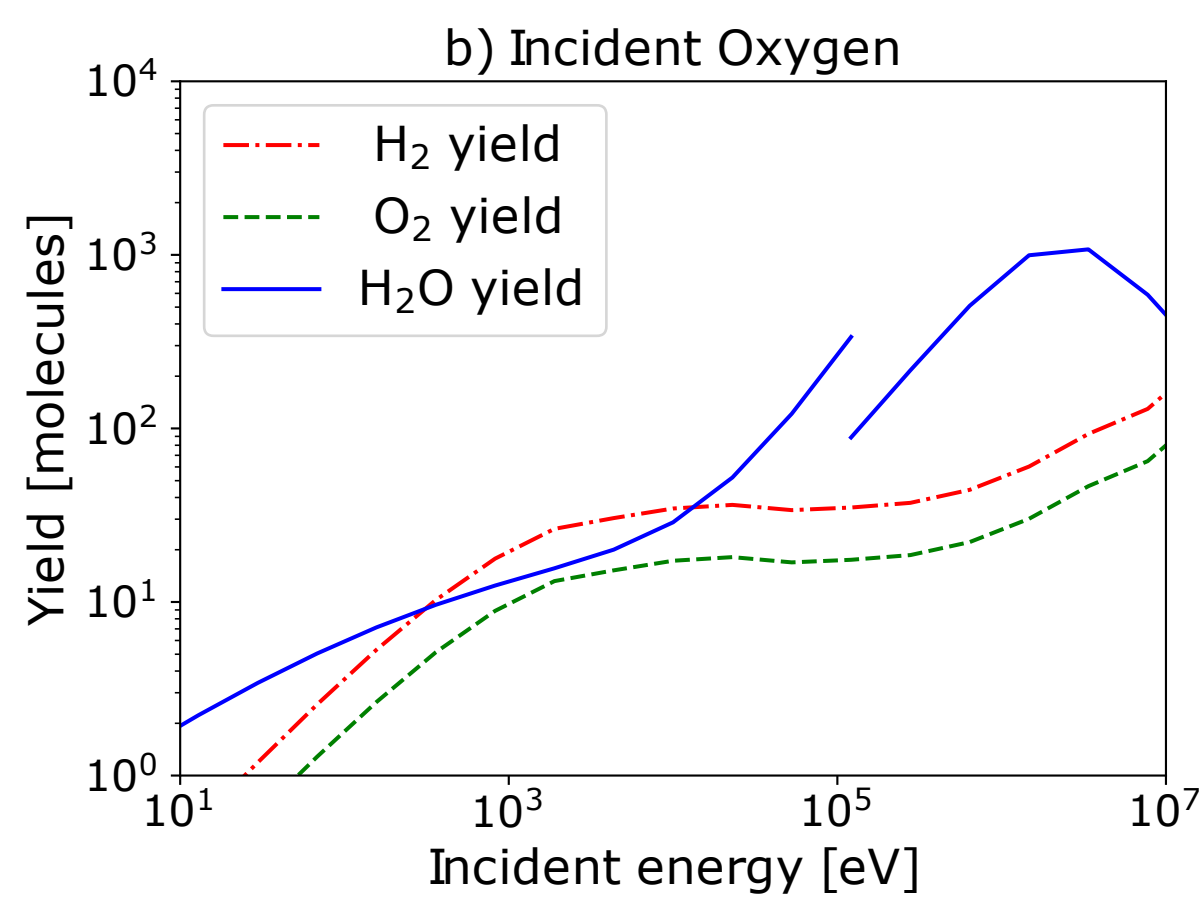
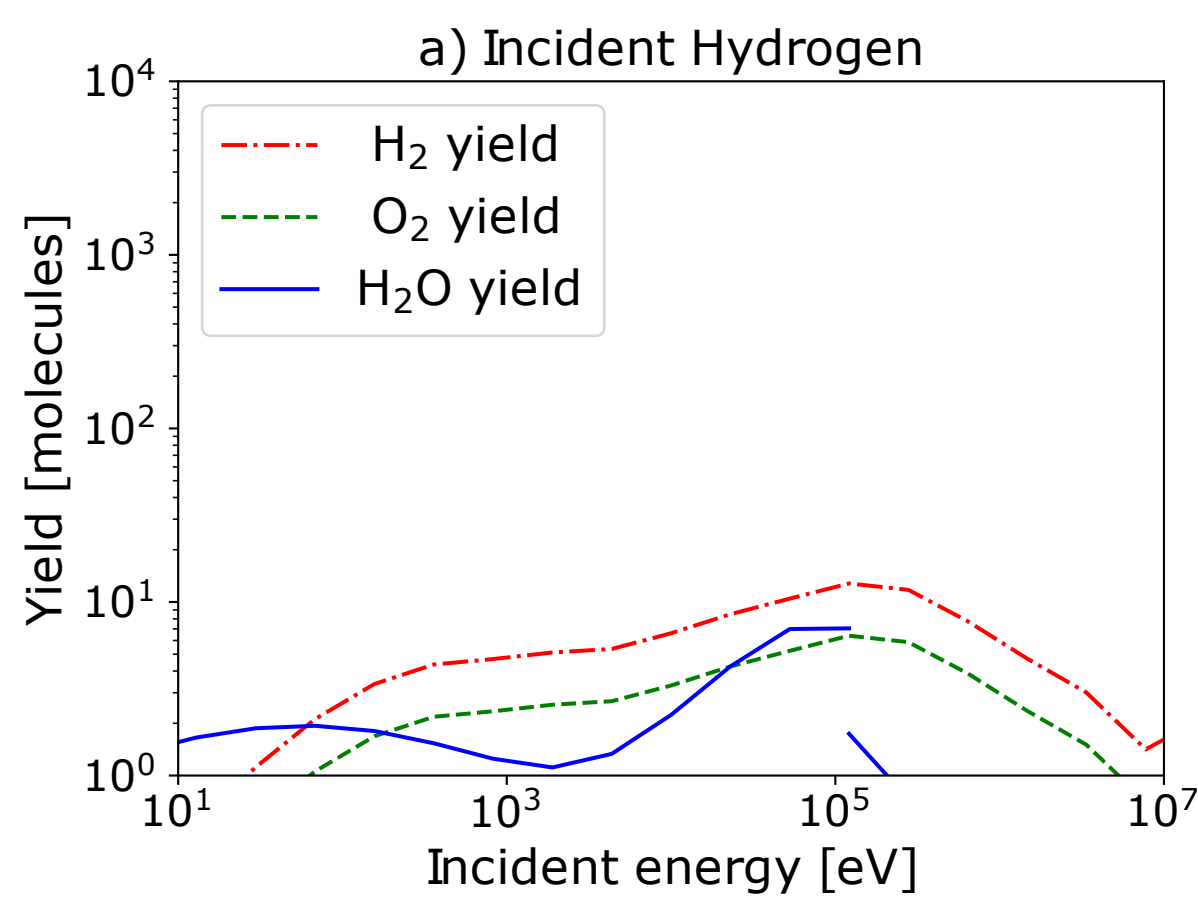
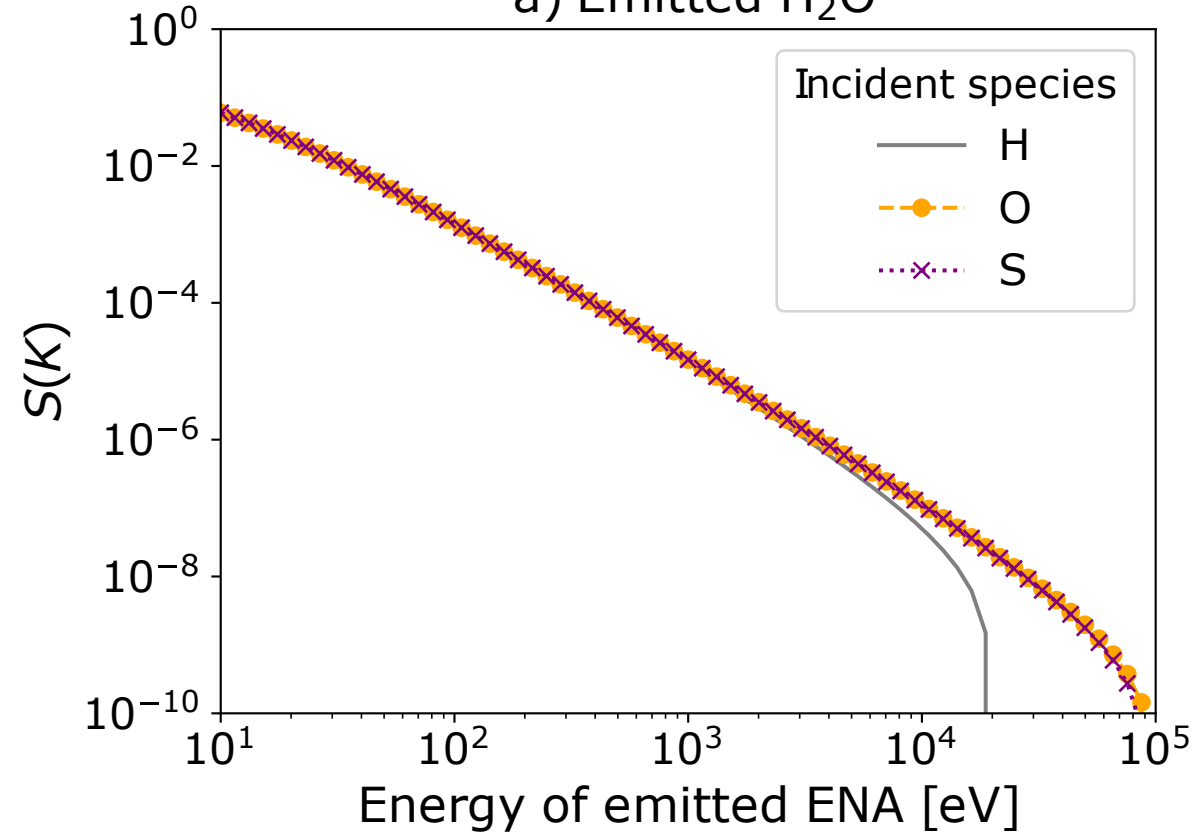


Figure 4.

a) Emitted H₂O

b) Incident H

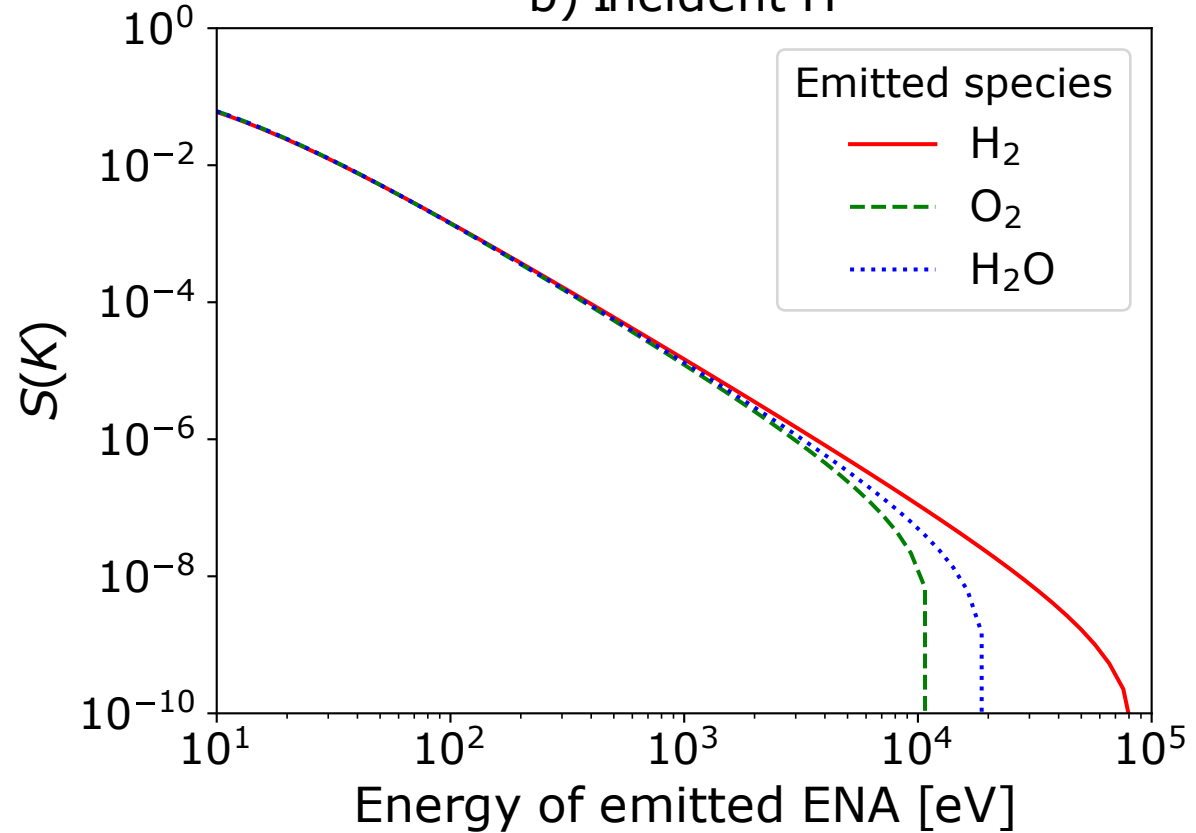


Figure 5.

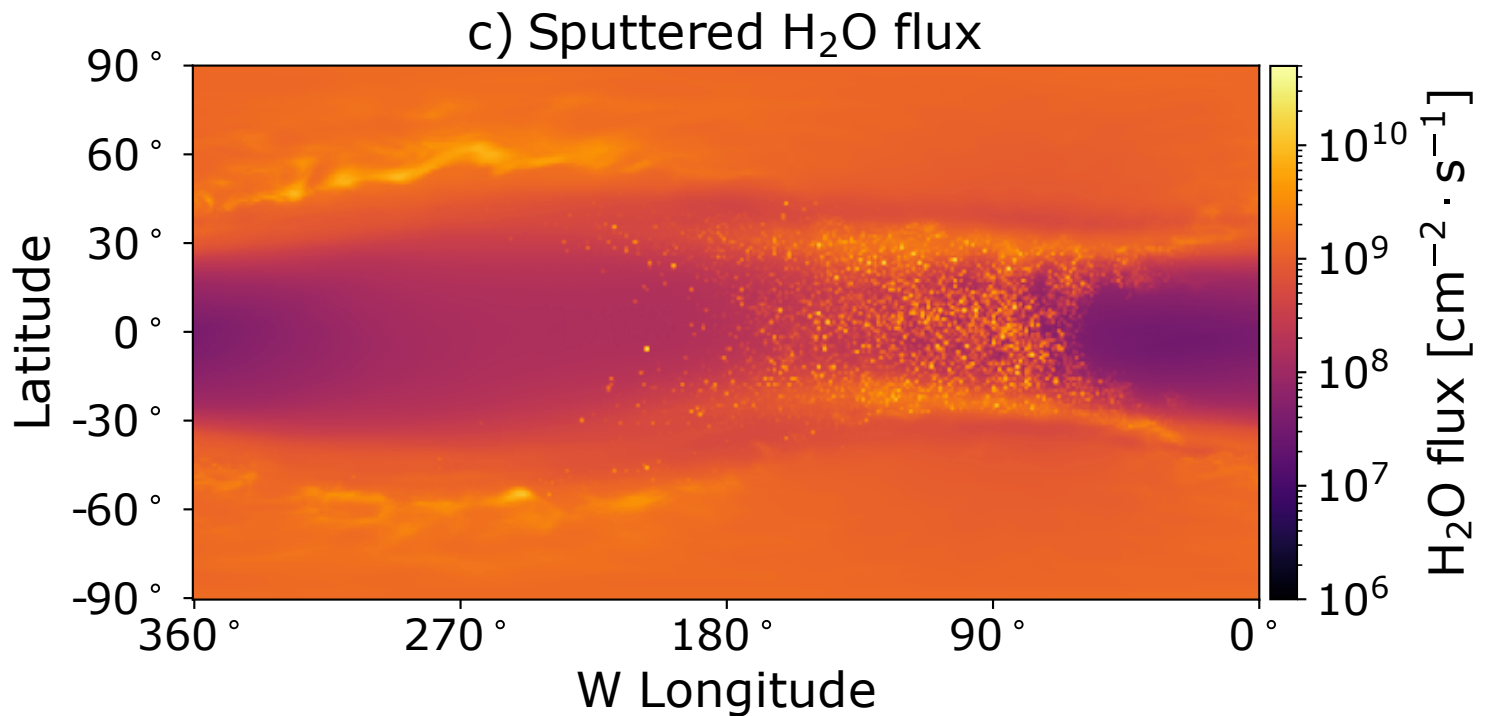
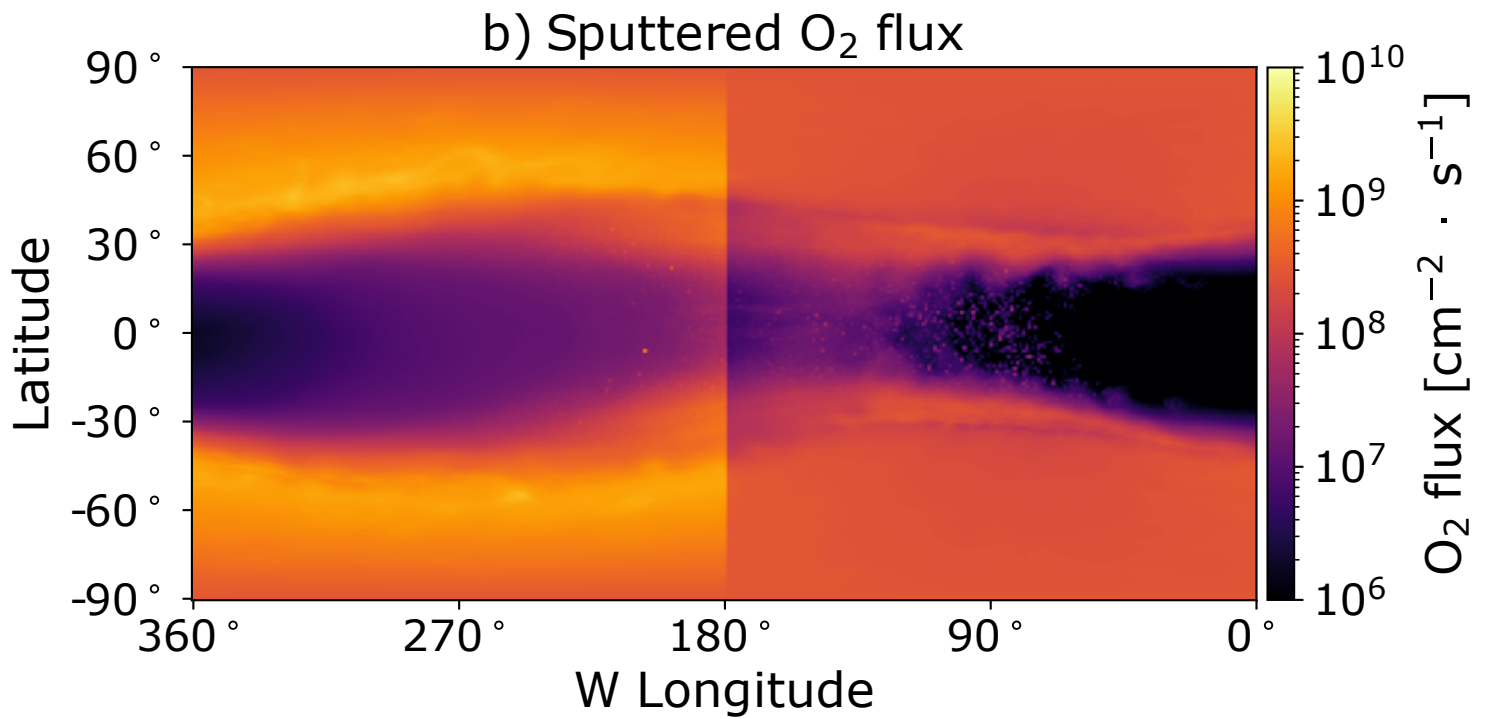
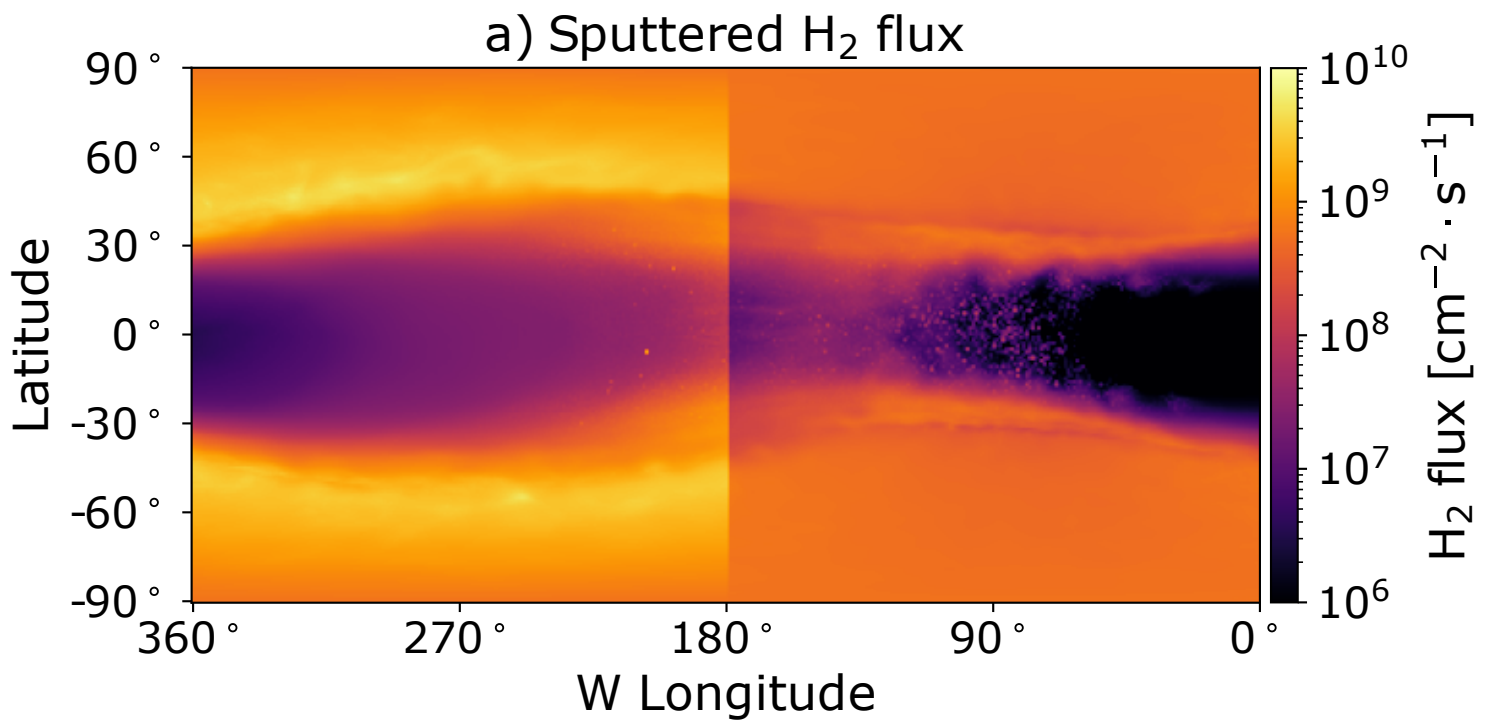
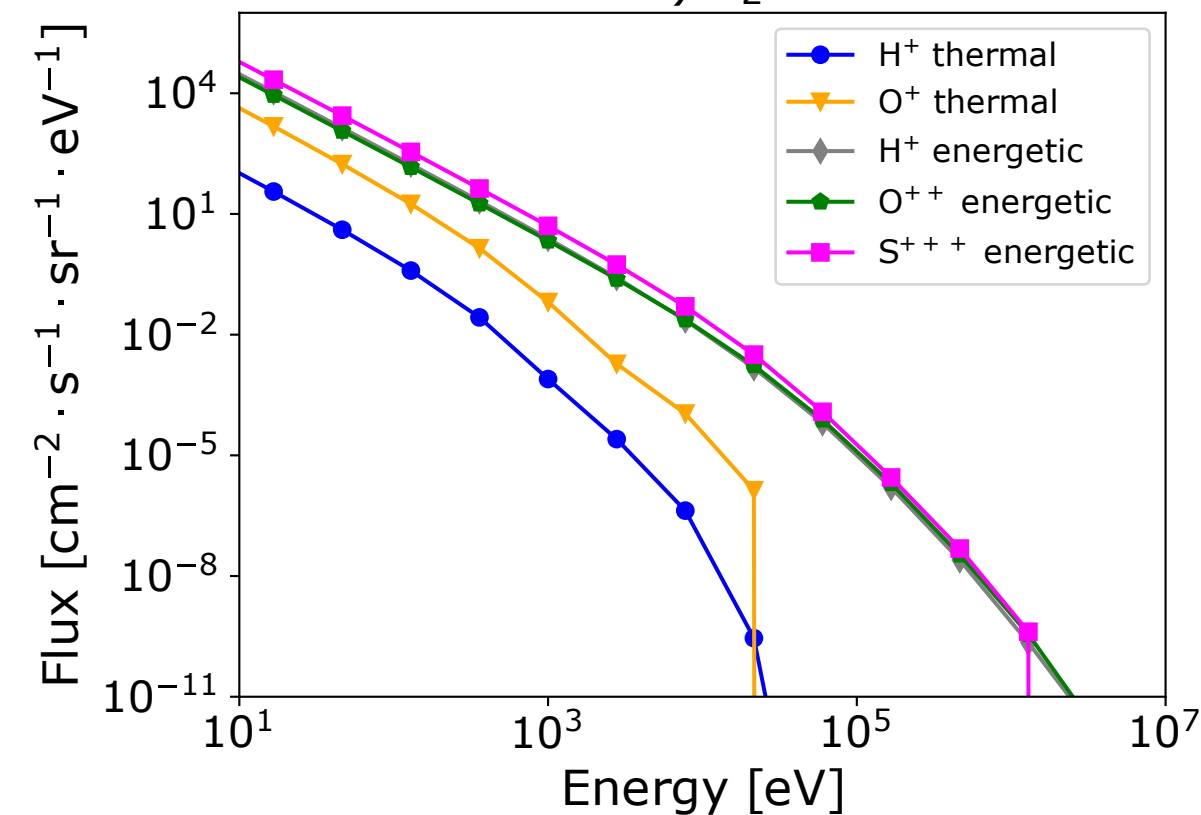
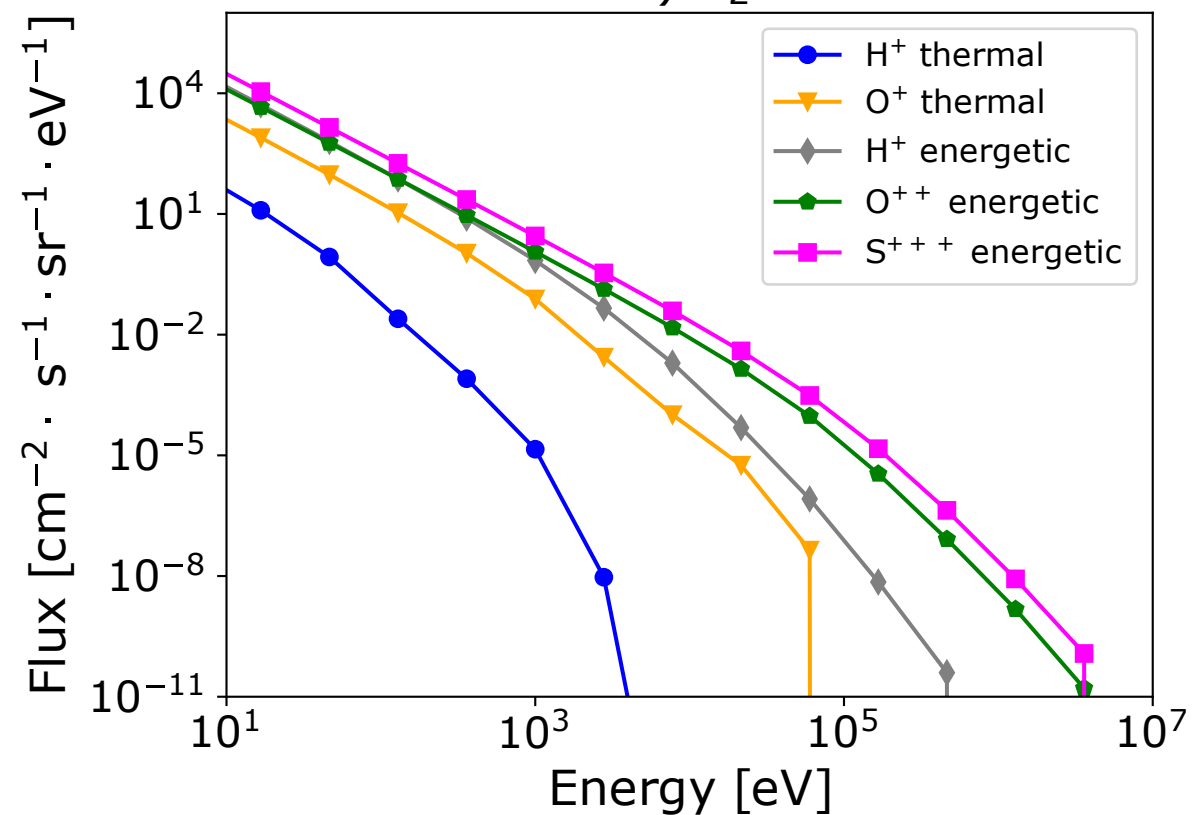
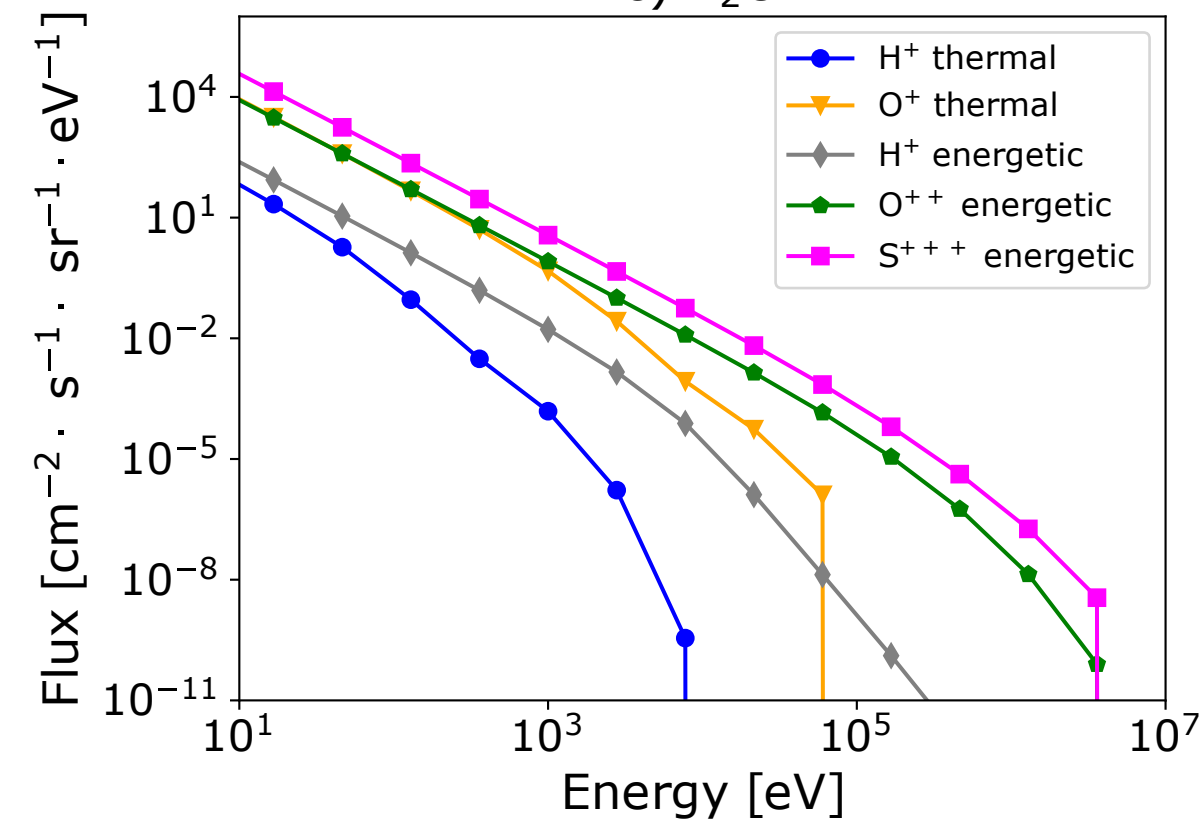


Figure 6.

a) H₂b) O₂c) H₂O

d) All ENA fluxes

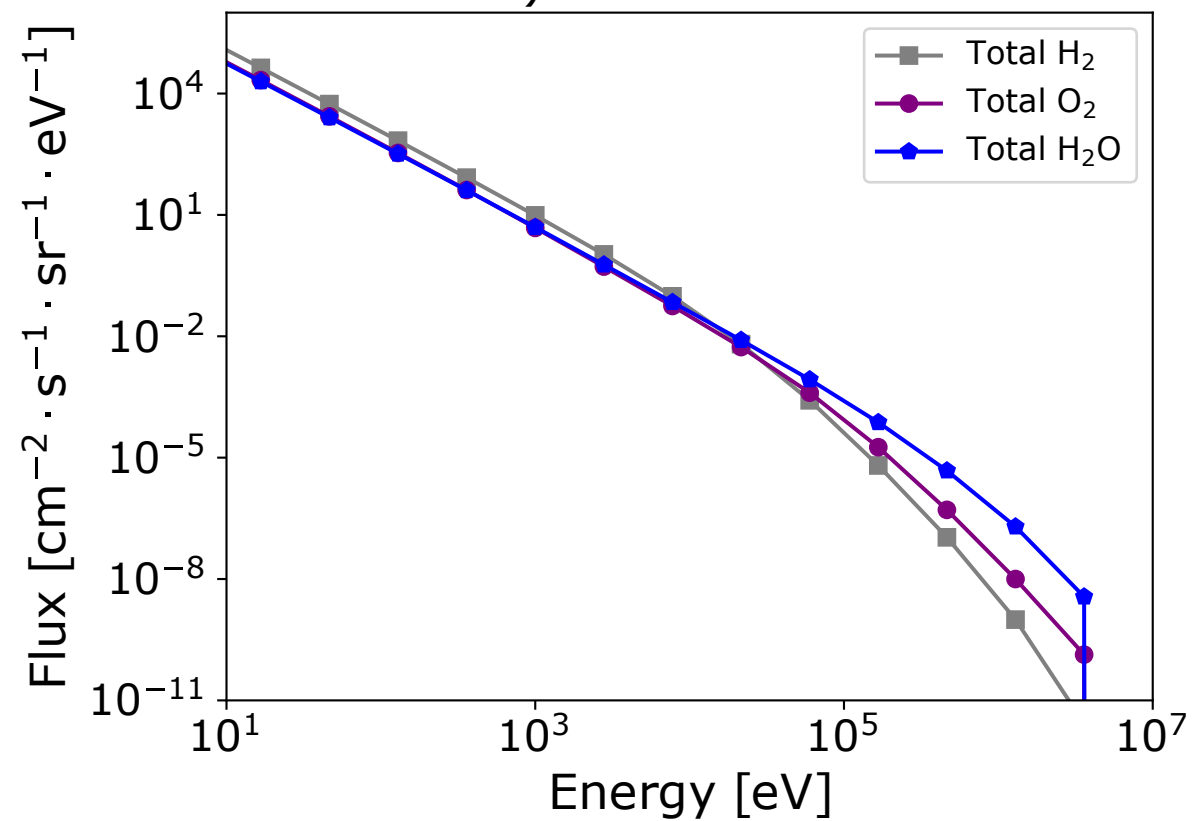


Figure 7.

Estimated JNA countrate

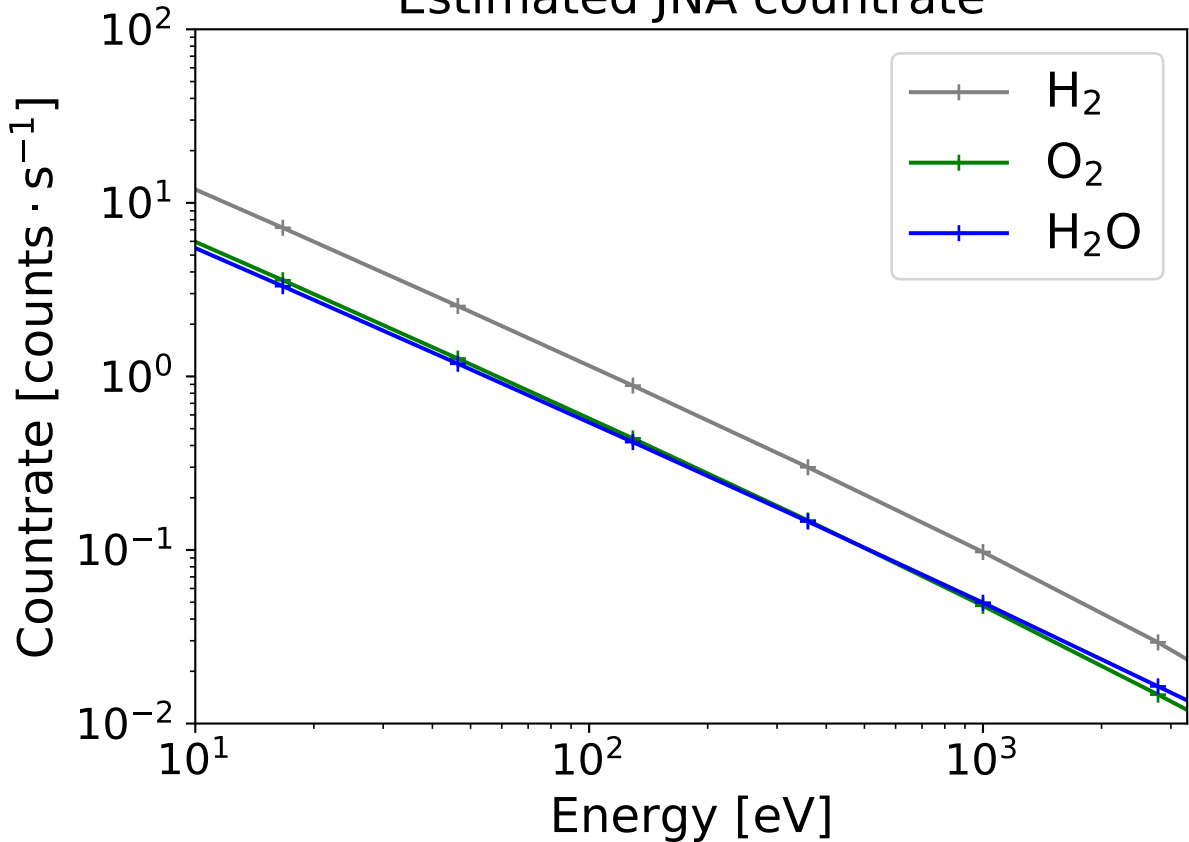


Figure 8.

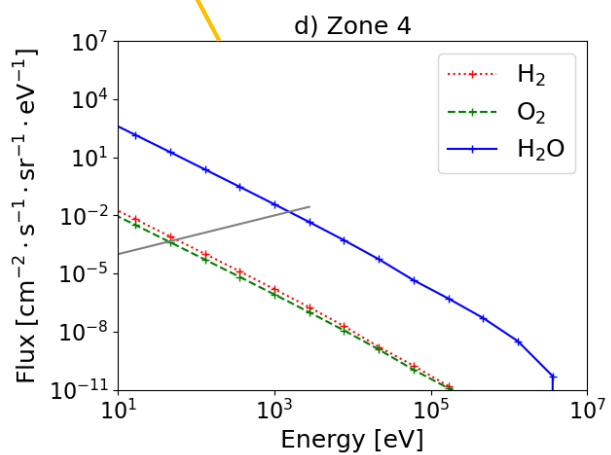
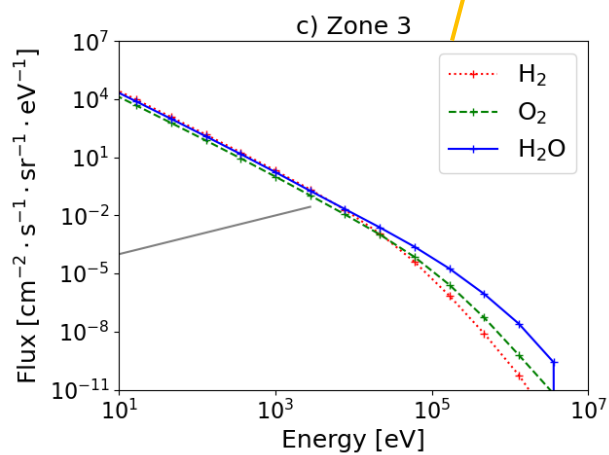
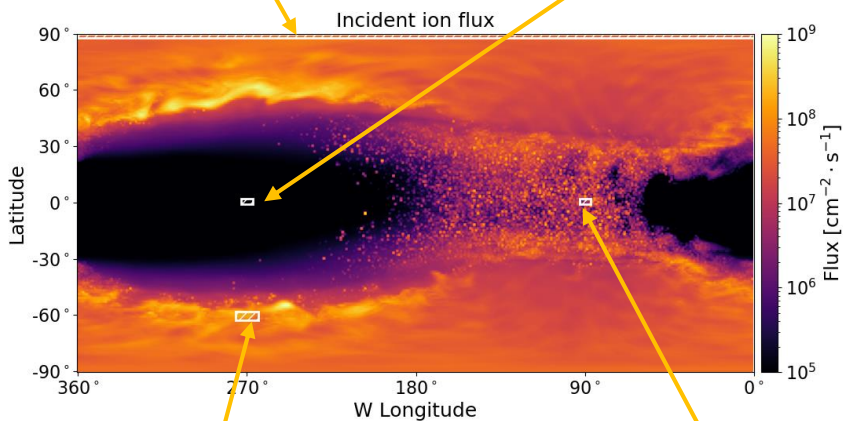
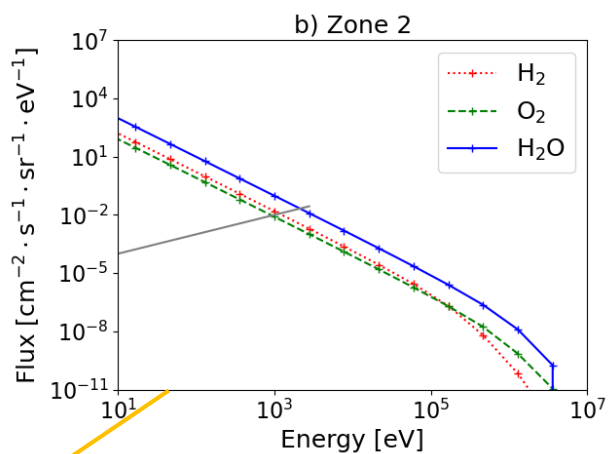
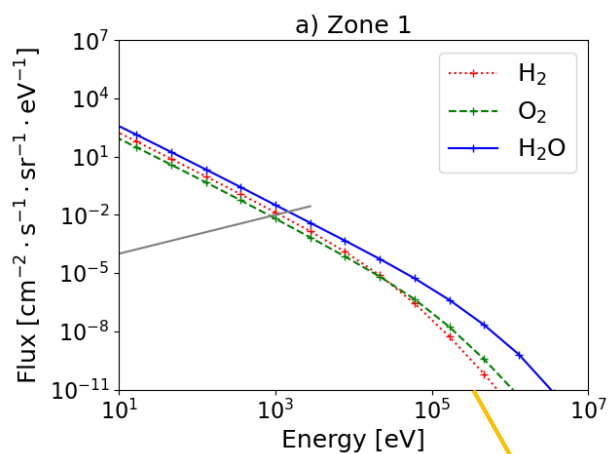


Figure 9.

H₂O

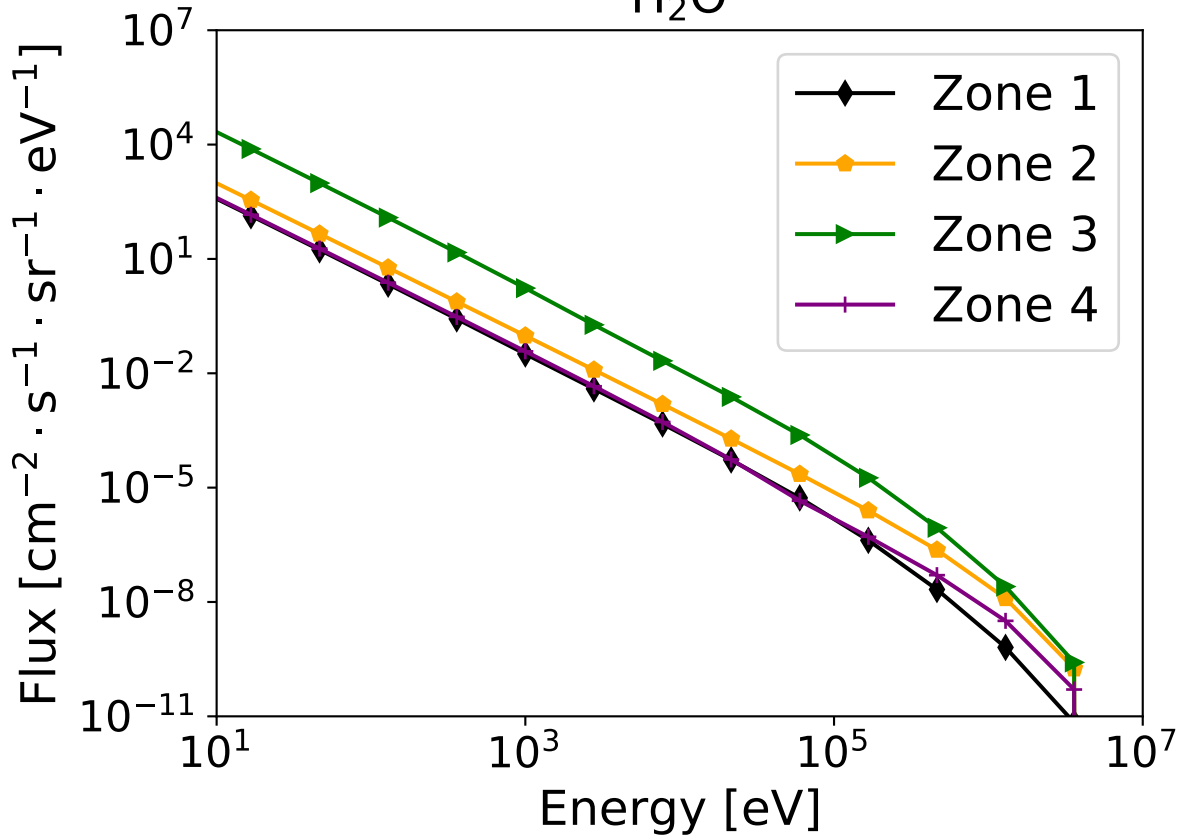


Figure 10.

